

## Review

## Computational insight into the bioapplication of 2D materials: A review

Yinyin Qian <sup>a,b,c</sup>, Huaming Yang <sup>a,b,c,d,\*</sup><sup>a</sup> Engineering Research Center of Nano-Geomaterials of Ministry of Education, China University of Geosciences, Wuhan 430074, China<sup>b</sup> Faculty of Materials Science and Chemistry, China University of Geosciences, Wuhan 430074, China<sup>c</sup> Laboratory of Advanced Mineral Materials, China University of Geosciences, Wuhan 430074, China<sup>d</sup> Hunan Key Laboratory of Mineral Materials and Application, School of Minerals Processing and Bioengineering, Central South University, Changsha 410083, China

## ARTICLE INFO

## Keywords:

2D materials

Bioapplications

Density functional theory calculations

Molecular dynamics calculations

## ABSTRACT

With the booming development of two-dimensional (2D) materials, their potential for optical, electrical, chemical, and biomedical applications is highly anticipated. Advances in the synthesis, characterization, and analysis of 2D materials have been made by leaps and bounds, while the microscopic mechanisms and dynamics of their bioapplications remain unclear. Theoretical computations, such as density functional theory (DFT), have become increasingly popular and powerful in the past few years due to the availability of high-speed computing devices. As a result, in the last few years, theoretical calculations have been pivotal in exploring the underlying mechanisms of two-dimensional materials for biological applications. These calculations potentially further improve theoretical models to anticipate different physicochemical features and biological consequences of 2D materials or forecast the microscopic details of 2D materials for bioapplications to supplement experiments. This review highlights theoretical calculations of 2D materials applied to bioimaging, biosensing, disease diagnosis, drug delivery, and disease treatment. In addition to classical graphene or 2D transition metal dichalcogenides, some 2D materials with good biocompatibility, such as natural lamellar materials (nanoclays), graphdiyne, Xenes, etc., are highlighted.

## Introduction

Layered structures that can be peeled off into single or several layers to form new nanomaterials are called two-dimensional (2D) materials. Typically, the thickness was only a few angstroms to a few nanometers, whereas the lateral dimensions might range from tens of nanometers to tens of micrometers or greater.<sup>[1]</sup> Their high lateral size to thickness ratio is caused by this characteristic. Nanomaterials are of great interest, such as graphene and its derivatives (including graphene oxide (GO) and reduced GO (rGO)), Xenes, hexagonal boron nitride (*h*-BN), transition metal dichalcogenides (TMDCs), natural layered clay materials, and so on.<sup>[2]</sup> Unusual mechanical strength, physicochemical features (such as photonic, catalytic, magnetic, electronic, etc.), and a range of fascinating functions have been observed in 2D materials. 2D materials exhibit great promise in a range of applications, from well-established energy storage conversion to emerging biomedicine.

Due to their huge "materials library," which provides a wide range to fulfill the demands of many biomedical applications, 2D materials for biomedical applications have advanced quickly. For instance, several 2D materials, such as phosphorene, MoS<sub>2</sub>, WSe<sub>2</sub>, and *h*-BN, offer a broad

range of light absorption owing to their highly adjustable band gaps, which facilitates their use in biosensing, bioimaging, and photodynamic treatment.<sup>[3–5]</sup> The large surface area is caused by their unique ultra-thin planar structure, which contributes to high drug delivery efficiency.<sup>[6]</sup> The majority of 2D materials also have strong biocompatibility and biodegradability, which makes it more accessible for them to be used in biomedicine.<sup>[7,8]</sup> More importantly, their satisfactory hydrophilicity and biocompatibility, abundant functional groups, and high electronic conductivity have been used as promising carriers for nanozymes, exhibiting excellent catalytic activity and stability, as well as expanding the utilization of 2D materials in biomedicine.

The strong development of biological applications of 2D materials, most of which combine experimental and theoretical approaches, fully illustrates the benefits of theoretical calculations. For instance, DFT calculations expose Cu clusters with excellent oxidase-like activity on 2D carbon-based carriers, providing insight into reaction mechanisms at the atomic level by calculating the potential energy surface along the reaction coordinates in chemical reactions.<sup>[9]</sup> It fills the gap between theory and macroscopic experiments and is commonly employed in reactions to investigate the kinetics and mechanisms of virtually all areas

\* Corresponding author at: Engineering Research Center of Nano-Geomaterials of Ministry of Education, China University of Geosciences, Wuhan 430074, China.  
E-mail addresses: hm.yang@cug.edu.cn, hmyang@csu.edu.cn (H. Yang).

of chemistry.<sup>[10]</sup> In parallel, MD simulations are a practical tool to study the kinetic properties of nanomaterials in biomedicine because of their ability to achieve thermodynamic equilibrium at constant pressure, constant temperature, and constant particle number. MD simulation of lipid extraction from hexagonal boron nitride (*h*-BN) nanosheets was performed, and lipid extraction occurs if the strength of BN dominates compared to the cell membrane, and vice versa.<sup>[11]</sup> The potential for lipid extraction was estimated using potential of mean force (PMF) calculations, and the temperature dependency of the thermodynamic visualizations connecting these free energy barriers to lipid extraction was made abundantly evident. It was discovered that *h*-BN may enter cell membranes, remove lipids from them, and then generate holes and compromise cell integrity. Meanwhile, MD simulations provide the calculation of kinetic effects like rate constants, transport characteristics, and absorption spectra as well as the energy and mass transfer in chemical processes.<sup>[12]</sup> These computational methods will be mainstreamed into biomedicine in the near future and have great potential for application.

This paper reviews the progress of research on 2D materials in biological applications using DFT/MD computational methods. In particular, this review will focus on work that predicts biological applications of 2D materials purely through theoretical calculations and on theoretical simulation studies that reveal their intrinsic mechanisms and interact closely with experiments (molecular-scale simulation studies that address the intrinsic mechanisms of experiments by mutual validation are the prominently cited studies). Additionally, opportunities and obstacles for the development of computational biomaterials for experimental development are further foreseen. This review aims to help researchers better understand experimental trends from a microscopic and theoretical perspective and to attract computational chemists to a deeper and broader study of this topic, which is promised to provide novel ideas for the further advancement of biocomputational two-dimensional materials.

## Overview of computation

### Computational methods

#### DFT calculation

First Principle, the principle that describes the interaction of nuclei and electrons in the process of solving the Schrödinger equation from the theory of quantum mechanics. Density Functional Theory (DFT) is a specific implementation of First Principle calculations, which eliminates the wave function and takes the electron density as the fundamental variable, thus in reducing the computational cost. DFT in biological applications allows the prediction of surface energy, charge transfer, work functions, energy band structures, molecular orbitals, reaction paths, and Frontier molecular orbitals of materials.

The commonly used exchange-correlation functional in DFT are: (1) LDA, Local Density Approximation, an early DFT functional based on the local nature of the electron density, which only considers the case where the gradient of the electron density is zero. LDA is widely used for structure and energy calculations for simple systems. (2) GGA, the generalized gradient approximation, is an improvement based on the LDA generalized function, which introduces the electron gradient correction information and considers the case where the gradient of the electron density is not zero, and thus has a better performance in calculating the properties of the system compared to LDA. It is worth mentioning that the PBE functional, which is commonly used in GGA, was proposed by Perdew, Burke, and Ernzerhof in 1996,<sup>[13]</sup> and is widely used in biosensing and nano-enzymatic calculations. (3) The hybrid functionals, which consists of a part of the exchange energy in the Hartree-Fock method and the exchange energy in the DFT, is more accurate for the intermolecular interactions, electronic structure, etc. The B3LYP function is the most common hybrid function. Therefore, hybrid functionals are more used in drug transport studies and help to improve

the accuracy of the interactions between drug molecules and carriers.

In addition to DFT functional, dispersion correction, or DFT-D, is a method used to exchange the dispersion correction of exchange functionals is also crucial in improving computational accuracy. This correction is mainly used to improve the accuracy in terms of intermolecular van der Waals (vdW) forces (dispersion forces) and noncovalent interactions. Currently, the DFT-D correction proposed by Grimme is more popular and its version has been updated four times.

Time-Dependent Density Functional Theory (TD-DFT) is an extension of DFT to the transient domain and is mainly used to calculate the excited state properties (spectroscopy, electronic excitation, fluorescence, absorption) of a system. TD-DFT is used to calculate the energy and wave functions of excited states by solving the time-dependent Schrödinger equation. Due to its ability to achieve objective accuracy at low computational cost, the TD-DFT method has been widely used in bioimaging research in recent years.

### MD calculation

The essence of MD is to solve Newton's equations of motion with respect to time to calculate the motion of each atom or molecule and to analyze the behavior of its molecular motion. The macroscopic properties of the system are then extracted by giving the relationship between microscopic quantities (coordinates and velocities of molecules, etc.) and macroscopic observable measurements (temperature, pressure, heat capacity of the system, etc.).

MD simulations use force fields to describe the interaction potentials between atoms and molecules in a molecular system, and therefore for a suitable force field is crucial for the simulation of the system. In general, various types of force fields have been developed to simulate different molecules. Common force fields are atomistic simulation studies (COMPASS),<sup>[14]</sup> chemistry at Harvard macromolecular mechanics (CHARMM),<sup>[15]</sup> Quantum Force Field (QMFF), consistent valence force field (CVFF)<sup>[16]</sup> and so on. In addition, CLAYFF<sup>[17]</sup> is mainly used for the calculation of clay mineral structures.

### Theoretical parameters for bioapplications of 2D materials

#### Adsorption energy

The adsorption energy is a common indicator of the strength of binding of the adsorbate to the substrate. This energy is calculated by the formula.

$$E_{\text{ads}} = E_{A+B} - E_A - E_B \quad (1)$$

where  $E_{A+B}$ ,  $E_A$ , and  $E_B$  represent the energies of the adsorption system, substrate, and adsorbent, respectively. If the adsorption is thermodynamically favorable, the energy of the whole adsorption system will be lower compared to the sum of the energy of the substrate and the adsorbate, resulting in a negative adsorption energy value. Depending on the magnitude of the adsorption energy value, it is possible to determine the system physisorption or chemisorption process. It is worth noting that in simulating the adsorption system to calculate the adsorption energy, the substrate, and the adsorbate must use the same exchange-correlation function to improve the comparability of the calculation. To perform geometric relaxation, there are usually three convergence criteria, i.e., energy, force, and atomic displacement.<sup>[18]</sup> Every substrate provides the possibility to provide several various adsorption sites and usually requires an adsorption site test prior to testing, where the adsorbate is most likely to adhere to the lowest energy site. In biosensing, drug delivery, etc., the calculation of adsorption energy is crucial, e.g., the appropriate size of adsorption energy to control anticancer drug doxorubicin (DOX) is not easily desorbed under neutral conditions, but easily released under weakly acidic conditions (tumor environment).<sup>[19]</sup>

### Electron transfer, the density of states, and frontier molecular orbitals

In contrast to experimental epiphenomena, theoretical calculations yield insights into the binding mechanisms analyzed at the orbital level. The different types of adsorption are determined by the amount of charge transfer between the adsorbent and the adsorbed material, and the charge transfer is greater for chemisorption processes than for physical adsorption processes. Mulliken charge,[20] Hirshfeld charge,[21] and Bader charge[22] analysis are helpful instruments to assess the level of charge transfer and primarily offer a quantitative charge transfer value. The charge density difference (CDD) function diagram is a visual charge transfer diagram that provides many nuances of the direction of charge flow and the amount of charge transfer. It is calculated by the following equation:

$$\rho_{\text{diffe}} = \rho_{A+B} - \rho_A - \rho_B \quad (2)$$

where,  $\rho_{\text{diffe}}$ ,  $\rho_{A+B}$ ,  $\rho_A$ , and  $\rho_B$  represent the charge density of the adsorption system, total, substrate, and adsorbent respectively. A partial density of states (PDOS) diagram is used to determine how electron orbitals interact. Spin polarization, -s, p, d, and f orbitals in the upper and lower spin channels, according to DOS data. Different sub-orbitals are plotted for a given orbit to gain more insight into the orbital interactions, for example, PDOS for the d orbital plots five sub-orbitals:  $d_{z^2}$ ,  $d_{xy}$ ,  $d_{xz}$ ,  $d_{yz}$ , and  $d_{z^2-y^2}$ . The molecular electrostatic potential (MEP) surface is a parameter for visualizing charge distribution and evaluating the long-range reactivity of molecules to electrophilic and nucleophilic reactants.[23–25] MEP was also used as a tool to describe and predict non-covalent molecular interactions that do not involve any charge transfer between interacting molecules.[26].

Frontier molecular orbitals (FMO), are called HOMO (highest occupied molecular orbital) and LUMO (lowest unoccupied molecular orbital). The ability to donate electrons is represented by HOMO as an electron donor and the ability to absorb those electrons is represented by LUMO as an electron acceptor, both of which are crucial components in the reaction process of molecules. Generally, systems with large HOMO-LUMO energy gaps present excellent kinetic stability and minimal chemical reactivity, and vice versa. For bioimaging materials, the HOMO-LUMO band gap is a measure of whether an excited electron transitions from the LUMO to the HOMO level. Additionally, by using the following Eqs. (3), (4), and (5), respectively, it is possible to calculate global reactivity indicators such as the electron potential ( $\mu$ ), hardness ( $\eta$ ), and global electrophilicity index ( $\omega$ ) using the energy gap between HOMO and LUMO.

$$\mu = 1/2(E_{\text{HOMO}} + E_{\text{LUMO}}) \quad (3)$$

$$\eta = -1/2(E_{\text{HOMO}} + E_{\text{LUMO}}) \quad (4)$$

$$\omega = \mu^2/2\eta \quad (5)$$

### Molecular interactions

Following the weak dispersion force increases with the number of atoms and molecular weight, the dispersion effect evolves into a significant factor in quantum chemical systems. Dispersion correction may greatly increase the precision of molecular properties. Accurate association free energies for the host system are provided by the van der Waals dispersion corrections in density functional theory (DFT-D) in combination with the comparatively large basis set. Interactions could be estimated extremely precisely at the DFT level by employing DFT-D functionals. EDA (energy decomposition analysis), NBO (natural bond orbital), QTAIM (quantum theory of atoms in molecules), and NCI-RDG (non-covalent interactions-reduced density gradient) analyses were utilized to determine the nature and severity of the adsorbent -carrier interactions and to reveal the nature of these interactions. Specifically,

The interactions that generate chemical bonds between molecular fragments or individual fragments were identified through EDA analysis. In EDA, the total bonding energy ( $\Delta E_{\text{bonding}}$ ) is divided into electrostatic ( $\Delta E_{\text{electrostatic}}$ ), kinetic ( $\Delta E_{\text{kinetic}}$ ), coulomb ( $\Delta E_{\text{coulomb}}$ ), and dispersion ( $\Delta E_{\text{dispersion}}$ ) energies. NBO analysis is the study of intra- and intermolecular bonding and bond interactions. On the basis of electron density, QTAIM defines a chemical bond as the route with the highest electron density, and is to be used to study weak interactions, especially hydrogen bonding interactions. It has been demonstrated that NCI can differentiate between hydrogen bonds, van der Waals interactions, and repulsive space interactions, and it gives a graphical portrayal of areas where non-covalent interactions take place in actual space. Atoms-in-molecule (AIM) analysis is an efficient technique for examining the characteristics of intermolecular interactions [27]. This method allows for the differentiation of molecular interactions based on topological factors.

### Radial pair distribution function

The radial pair distribution function (RDF) evaluates the adsorption behavior of drug molecules. Understanding the preferred binding locations of adsorbed molecules and the interaction distances with the carrier is made easier with the use of RDF plots. The following equation determines the probability of the distribution of atom ( $\beta$ ) at a certain distance ( $r$ ) around a reference group of atoms ( $\alpha$ ) in RDF.

$$g_{\alpha\beta}(r) = \frac{V}{N_\alpha N_\beta} \left( \sum_{i=1}^{N_\alpha} \frac{n_i \beta(r)}{4\pi r^2 \Delta r} \right) \quad (6)$$

where  $N$  is the number of particles;  $n_i \beta(r)$  is the total number of atoms  $\beta$  in the spherical distance  $r$  from atom  $\alpha$ ; and  $V$  is the volume of the simulation box.

### Root mean square displacement

The root mean square displacement (RMSD) describes the deviation from the original structure of MD after simulation, and its value reflects the degree of each atom in the system deviates from the original position.

$$\text{RMSD} = \sqrt{\frac{1}{N} \sum_{i=1}^N \delta_i^2} \quad (7)$$

where  $\delta_i$  is the position offset of the  $i$  th atom at some time (absolute value of the difference between the present position and the original position).

### Advances in the calculation of nanoclays for bioapplications

#### Physical characteristics of nanoclays

Nanoclays are inorganic minerals produced naturally and are categorized into many groups depending on their chemical composition and morphology, including montmorillonite, kaolinite, and halloysite.[28] Clay minerals all have a natural two-dimensional structure of sheet-like geometry. These phyllosilicates are sheet-structured hydrous silicates (clay minerals) that occasionally include water along with elevated quantities of cations such as  $\text{Mg}^{2+}$ ,  $\text{K}^+$ ,  $\text{Na}^+$ , and  $\text{Ca}^{2+}$ .[29] The main characteristics and physical properties of these minerals are described in the following.

Montmorillonite is a collection of silica-aluminate layered minerals with exceptional composition and powerful physicochemical properties at low cost and abundant reserves (Fig. 1a).[30] MMT is a layered aluminosilicate mineral with three structural units, where a layer of the central octahedral sheet ( $\text{AlO}_6$ ) is sandwiched between two layers of tetrahedral sheets ( $\text{SiO}_4$ ). MMT is a layered aluminosilicate mineral with three structural units, where a layer of alumina octahedral sheets is

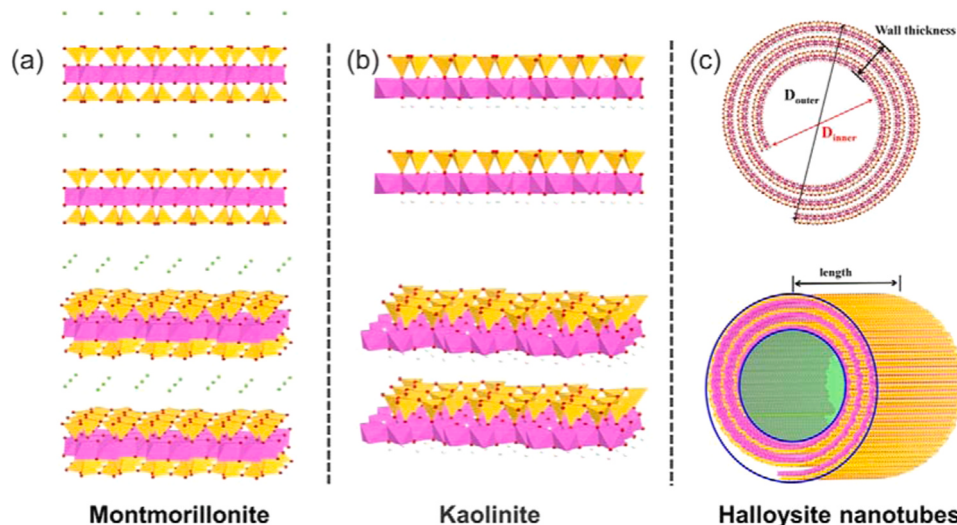


**Fig. 1.** Structure of a) Montmorillonite, b) Kaolinite, and c) Halloysite nanotubes. c) Reproduced with permission.[193] Copyright 2021, Elsevier.

sandwiched between two layers of silica tetrahedra.[31] Isomorphous substitutions in the MMT crystal structure, such as the substitution of  $\text{Al}^{3+}$  by  $\text{Mg}^{2+}$  in the octahedral position and  $\text{Si}^{4+}$  by  $\text{Al}^{3+}$  in the tetrahedral position, produce a net negative surface charge.[32] Notably, montmorillonite is biologically inert and can be removed from the body effortlessly.[33].

Kaolinite (Kaol) is a mineral in the kaolinite group that has a 1:1 layered structure (Fig. 1b). Specifically, a 0.7 nm thick layer is formed by combining a silica tetrahedral sheet ( $\text{SiO}_2$ ) with an alumina octahedral sheet ( $\text{Al(OH)}_3$ ). The basic oxygen atoms of the tetrahedral sheet form only one surface of the kaolinite layer, while the oxygen atoms of the octahedral sheet form the other surface.[34] Kaolinite has different charges on the basal plane, two surfaces are usually negatively charged due to its isomeric substitution, while the protonation or deprotonation formed by the broken bonds of the structure at its edges causes different charges. This charge difference is tightly connected to pH, and the substitution and pH environment of kaolinite has a major influence on its characteristics.[35] The nature of kaolinite has responsible for a broad variety of biological applications, where it has been found to be an active ingredient for the therapy of common diseases. It may also be employed in drug delivery systems to load a range of medications, manage the qualities of formulations, and increase the biocompatibility of active substances by virtue of its highly compatible surface that allows for ready modification.[36].

Halloysite is a 1:1 layered silicate clay mineral similar to kaolinite, and its morphology is affected by the extraction site (Fig. 1c).[37] It is an abundant and cost-effective clay that could be found in enormous amounts all over the world, including China, the United States, Belgium, France, and New Zealand.[38] Typically, Halloysite nanotubes (HNT) are single tubes ranging from submicron to a few microns in length, usually less than 100 nm in diameter, with the inner cavities forming cylindrical voids ranging from 5 to 30 nm in diameter.[39] HNTs have Al-OH flakes on the inside and Si-O flakes on the outside resulting in a completely different chemistry between the lumen and the outer surface of the tube. The inner surface is positively charged due to the protonation of Al-OH groups under acidic conditions. However, at pH values above 2, the Si-OH groups are gradually deprotonated, resulting in an excess of negative charge on the outer surface. The charge separation of HNTs and the special hollow tubular structure make this clay mineral very suitable for biological applications. According to cytotoxicity studies of HNTs, HNTs are nontoxic, well-biocompatible, and environmentally friendly.[40].

#### Theoretical investigation of nanoclay-based materials for bioapplications

Nanoclays with nanoscale layers are natural two-dimensional materials extracted from ore and have been commonly used as a corner of medical formulations since ancient times.[41] With their unique morphology, good biocompatibility, abundant surface hydroxyl groups, [42] and high loading capacity,[43] they have been developed for the delivery of various therapeutic drugs. The most commonly used nanoclays in medicine are HNTs, Kaol, and MMT.

Due to the complexity of clay, it remains a mystery whether drug molecules are loaded onto the clay surface or between the clay layers, and whether drug-clay interactions are more favorable will also be studied. In order to understand the mechanism of drug loading in clay, theoretical calculations will assist at the atomic level. For example, Karataş et al. investigated the adsorption of curcumin anticancer drugs on montmorillonite (MMT), performing DFT and MD simulations in an amphiphilic polymer (PLGA) and the aqueous environment under acidic/neutral conditions.[44] MMT has been found to have a high affinity for polymer or drug molecules, especially due to vdW interactions (Fig. 2a). Excitingly, MMT has been observed to promote curcumin release. Yang et al. analyzed the DOX loading mechanism by combining the DFT calculation results of kaolinite (Kaol) and MMT.[45] Fig. 2b show that Kaol was able to stably adsorb DOX on both surfaces, with adsorption energies of  $-2.38$  eV (on the Si-O surface) and  $-3.73$  eV (on the Al-OH surface), indicating that DOX adsorption was more favorable on the Al-OH surface. The adsorption energy of DOX on the Si-O plane of MMT is  $-2.72$  eV, which indicates that DOX binds Kaol more closely than MMT. Interestingly, calculations of the adsorption energy between colenteric acid, 5-aminosalicylic acid (5-ASA), and Kaol's aluminol and siloxane surfaces suggest that 5-ASA has a greater affinity for aluminol surfaces, so Kaol is a promising 5-ASA drug carrier. [46] The molecular structure and crystal structure of capsaicin, an anticancer and anti-inflammatory drug, were calculated and proved to be beneficial to the adsorption of montmorillonite in the interlayer space.[47] Two laminated clays (a natural Wyoming montmorillonite (marketed as Cloisite®Na; Mt) and a synthetic hectorite (which is referred as Laponite®XLG; Lap) to cover the type II diabetes oral drug metformin (MF).[48] The results show that the cationic exchange reaction between MF and the interlayer produces a thermodynamically favorable system, in which the MF substance forms a single layer in the interlayer of the two clays, and the Lap is more conducive to the adsorption of MF.

Kaolinite edge surfaces have a more complex structure and more subtle chemistry. The clay surface was discovered to limit Gram-

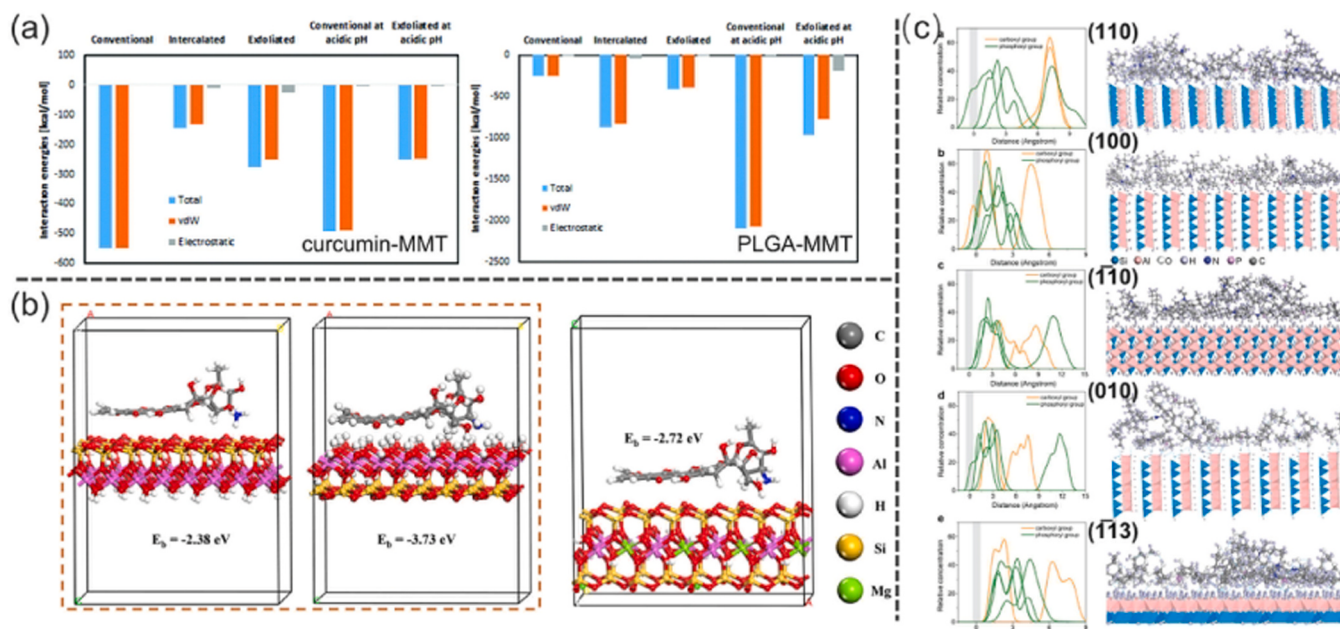


**Fig. 2.** a) Interaction energy of curcumin-MMT and PLGA-MMT under neutral/acidic conditions. a) Reproduced with permission.[44] Copyright 2017, Royal Society of Chemistry. b) Surface adsorption of DOX on Kaol and MMT. b) Reproduced with permission.[45] Copyright 2022, American Chemical Society. c) Atomic concentration distribution of carboxyl and phosphorus groups on Kaol with different crystal surfaces. c) Reproduced with permission.[49] Copyright 2023, Wiley.

negative bacteria growth via lipopolysaccharide (LPS) binding. Yang et al. demonstrated the antibacterial mechanism of the kaolinite edge surface against Gram-negative bacteria through a combination of experimental and simulation studies.[49] Transmission electron microscopy (TEM) results demonstrated that the cell membranes of the rim surfaces of kaolinite were significantly damaged upon contact with Escherichia coli (*E. coli*). Moreover, both Fourier transform infrared (FTIR) spectroscopy and X-ray photoelectron spectroscopy (XPS) results confirmed the interaction between *E. coli* and the edge surface of kaolinite. DFT/MD calculations were further performed to explain the direct contact antimicrobial mechanism at the atomic level. Notably, LPS exhibits strong hydrogen binding to the kaolinite edge surface and has a folded structure (Fig. 2c). In particular, the carboxyl and phosphorus groups of the lipopolysaccharide, particularly the phosphorus group, engage significantly with the various crystalline surfaces of the kaolinite edge. Following the contact process, membrane tension may cause mechanical deformation, resulting in cell rupture and death.[50] This behavior is analogous to the "phospholipid sponge effect" contact killing mechanism, which occurs by the preferential attachment of negatively charged phospholipids from the bacterial cell membrane to the positively charged surface of the nanoclays.[51].

Because of the complexity of clay structures, calculations for applications in biology require the selection of appropriate functional or computational methods. Periodic DFT calculations are unable to adequately model the behavior of complex systems (e.g., large drug molecules loaded on clay surfaces), and MD simulations avoid this problem by using less accurate but very fast molecular mechanics. However, for MD simulations of clays, the choice of appropriate force fields gives more accurate results for the interaction between drug molecules and carriers or between clays and cell membranes, and the combination of experimental phenomena shows the advantages of computational excellence.

## Advances in the calculation of carbon-based materials for bioapplications

### Structure and electronic properties of carbon-based materials

Carbon is the fundamental component of life and the foundation of all organic chemistry. Carbon-based materials display an unlimited number of distinct structures and a wide range of physical characteristics attributed to the diversity of carbon bonding.[52] These physical properties are determined to a large extent by the dimensionality of these structures. In the system of carbon atoms, two-dimensional isomers of carbon (e.g. graphene, graphdiyne, graphene oxide, etc.) play an essential role at the theoretical and experimental level.

A honeycomb lattice of 2D carbon atoms with the thickness of a single atom is called graphene.[52] Since it was first reported in 2004, this  $sp^2$  hybridized carbon material has opened up a diversity of interesting applications for the field of chemistry, physics, and materials science, from basic science to industrial applications.[53] The band structure of graphene at the Fermi level is a bandgap free Dirac point (Fig. 3a).[54].

Graphene oxide (GO) is a honeycomb-like plane of  $sp^2$  and  $sp^3$  hybridized carbon atoms with many oxy-functional groups such as epoxy (-O-) and hydroxyl (-OH) groups randomly distributed on the surface, while carboxyl (-COOH) and carbonyl (-C = O) groups are present at the edges.[55] As shown in Fig. 3b, the -O- and -OH groups are near each other and the energy band of graphene oxide is changed compared to graphene, e.g., the displacement of Dirac  $\delta$  point leads to a narrow bandgap of 0.108 eV.[55].

The two-dimensional sheet structure of graphdiyne (GDY) consists of benzene rings ( $sp^2$  hybridized carbon) and acetylene bonds ( $sp$  hybridized carbon) (Fig. 3c). The  $2p_z$  orbital overlap of carbon atoms in GDY and the inhomogeneous  $\pi$ -bonds formed by  $sp^2$  and  $sp$  hybridization created a gap.[56] Compared to the zero band gap of graphene, the monolayer GDY has a narrow direct band gap and is semiconducting, with a bandgap ranging from 0.44 to 1.47 eV based on previously reported DFT results.[57,58].

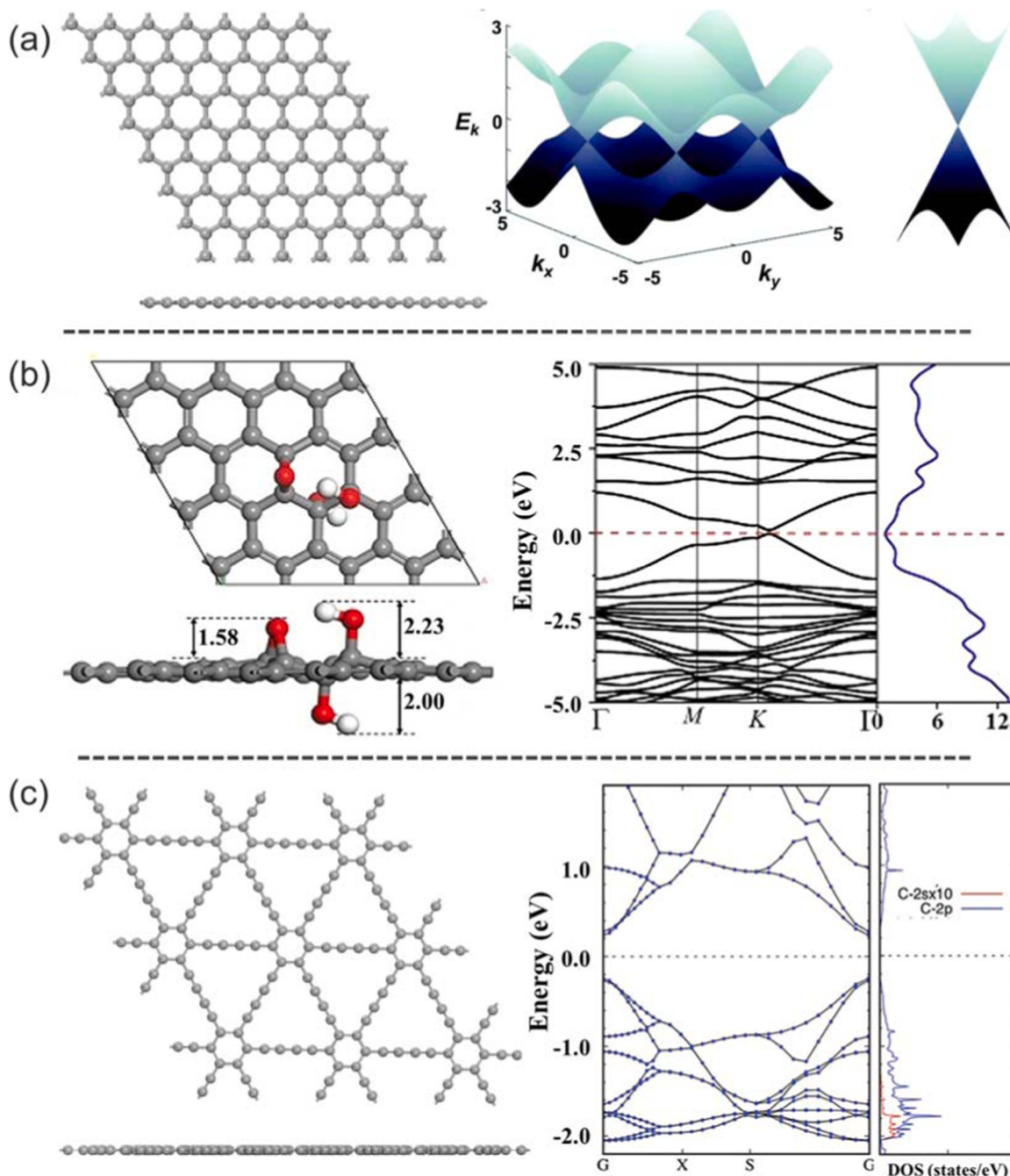


**Fig. 3.** Structure and band structure of a) graphene, b) graphene oxide, and c) graphdiyne. a) Reproduced with permission.[54] Copyright 2018, Royal Society of Chemistry. b) Reproduced with permission.[55] Copyright 2023, Elsevier. c) Reproduced with permission.[58] Copyright 2021, Wiley.

#### Theoretical investigation of carbon-based materials in bioapplications

##### Computational carbon-based materials as biosensors

The biosensing mechanism is fundamentally one in which the interaction between the sensor sensitive material and the analyte is recognized and converted into a usable signal output. Thus the architecture of the sensor will change depending on the signal, which is diverse in nature such as temperature, light, chemical composition, etc. [59] 2D materials with prominent large specific surface areas are prominent in biosensors. At the atomic/electronic level, the contact between biomolecule and 2D sensitive substrate causes variations in properties such as resistivity, light absorption, electronic or optical bandgap, resulting in many detectable signals. In most cases, the generation of these signals mainly involves electronic and orbital changes,

which are the core component of sensing.[60] With their excellent electronic properties and biocompatibility, 2D carbon-based materials have an outstanding potential to be used in the fabrication of biological devices.[61] Theoretical simulations have paved the way for a deeper understanding of the detection of drinking capture of specific signals by biosensors and the changes in electronic structure induced by the recognized molecules on the sensitive material of the sensor.[62].

Human exhaled breath contains volatile organic compounds (VOCs) such as some specific ketones, acids, and aldehydes as markers for disease analysis, which is a new direction for efficient, convenient, sensitive and non-invasive medical diagnosis. Carbon-based materials are promising for the development of room temperature gas sensors. Since pristine graphene exhibits low sensitivity and selectivity,[63] defects, doping and other means can be used to improve the sensing performance

of graphene. For example, the adsorption of Pt-functionalized graphene [64] on ethyl butyrate as well as the adsorption of Pd, Pt, and Ag-functionalized graphene [65] on heptanal exhibited a significant change in the electronic properties, and ethyl butyrate and heptanal were used to detect COVID-19. Aasi et al. reported that graphene-like boron carbon nitride ( $\text{BC}_6\text{N}$ ) with C defects exhibited physisorption of acetone, ethanol, methanol, formaldehyde, toluene, carbon dioxide and water. In addition, the defective  $\text{BC}_6\text{N}$  sensor has a short recovery time for VOCs. [66] However, the adsorption of VOCs did not induce changes in the electronic structure, such as energy band structure and density of states. The current-voltage ( $I$ - $V$ ) response results derived from DFT combined with non-equilibrium Green's function (NEGF) indicated that the defective  $\text{BC}_6\text{N}$  exhibited high sensitivity only for ethanol, making it suitable for breath analysis of alcohol. Aasi et al. further found that the Pd modification resulted in a significant increase in the adsorption energy of  $\text{BC}_6\text{N}$  for exhaled gases (e.g., NO,  $\text{NO}_2$ ,  $\text{NH}_3$ , CO,  $\text{CO}_2$ ,  $\text{H}_2\text{S}$ , and  $\text{SO}_2$ ), resulting in chemisorption. [67] The  $I$ - $V$  response showed that the Pd-modified  $\text{BC}_6\text{N}$ -based sensors exhibited high sensitivity (98.6–134%) and selectivity (12.3–74.4 fold) for  $\text{NO}_x$  gas molecules and were insensitive to the interfering gases  $\text{H}_2\text{O}$  and  $\text{CO}_2$ .

Among the many 2D carbon isomers that are also emerging as biosensors, graphyne (GY) is one of the most promising materials. [68] The most widely studied are graphdiyne (GDY) and  $\gamma$ -graphyne ( $\gamma$ -GY), which are composed of  $\text{sp}^2$  and sp hybridized carbon. The difference is that in  $\gamma$ -GY, the hexagonal carbon rings are connected to each other by a single alkyne bond, whereas in GDY, the carbon rings are connected to each other by two alkyne bonds. Furthermore, a new carbon allotrope, bis-graphene, consists of hexagonal carbon rings with vinyl bonds and AA stacks, and this bilayer structure is similar to the aforementioned  $\gamma$ -GY as seen in the top view. Nadafan and coworkers reported the potential ability of  $\gamma$ -graphene and twin-graphene sheets to detect benzene, styrene, aniline, and o-toluidine, which are typical lung cancer

breathing gases. [69] DFT-PBE calculations showed that these gases were physically adsorbed onto  $\gamma$ -graphene and twin-graphene and possessed fast recovery rates. The adsorption of the VOCs onto  $\gamma$ -graphene (from 0.43 eV to 0.41–0.33 eV) and twin-graphene (from 0.7 eV to 0.62–0.27 eV) reduced the energy band gap and increased the electric dipole moment. Twin-graphene has been found to be more sensitive to sensitive to changes in the electronic properties of VOCs adsorption than  $\gamma$ -graphene's, and twin-graphene shows greater promise for use in breath sensors for lung cancer.

The development of efficient glucose biosensors for rapid and accurate monitoring of blood glucose has attracted widespread interest. Sakr and coworkers investigated the response of graphene and Pt-functionalized graphene to D-glucose adsorbent by GGA-PBE functional of DFT. [70] As shown in Fig. 4a, there was charge transfer between graphene sheets on Pt substrate adsorbing d-glucose molecules. This provides the fundamental theoretical basis for the establishment of glucose biosensors. The exchange-correlation between the local density approximation (LDA) of the DFT and the Perdew-Zunger (PZ) functional was used to functionalize boronic acid derivatives (BAs) on the surface of graphene (G) as a Glucose molecular detection sensor platform (BAs-G). [71] The results showed that BAs derivatives (4-formylphenylboronic acid (FPBA), 3-aminophenylboronic acid (APBA), thiophene-3-boronic acid (TPBA), 4-mercaptophenylboronic acid (MPBA)) were physisorbed/chemisorbed on the surface of graphene. Simulation results showed that BAs-G interacted with the diol groups of Glu to form covalent bonds and provide sensing signals by modifying the intensity of density of states (DOS) peaks of the sensing platform. When detecting Glu molecules by BAs-G molecules, it has been observed that MPBA-G has higher binding energy and interacts most frequently with Glu, and the change in electronic structure also indicates that glu exhibits good sensitivity and selectivity in MPBA-G. The effect of N, O, and Cl ion doping on graphene (G) as a D-glucose sensor was further

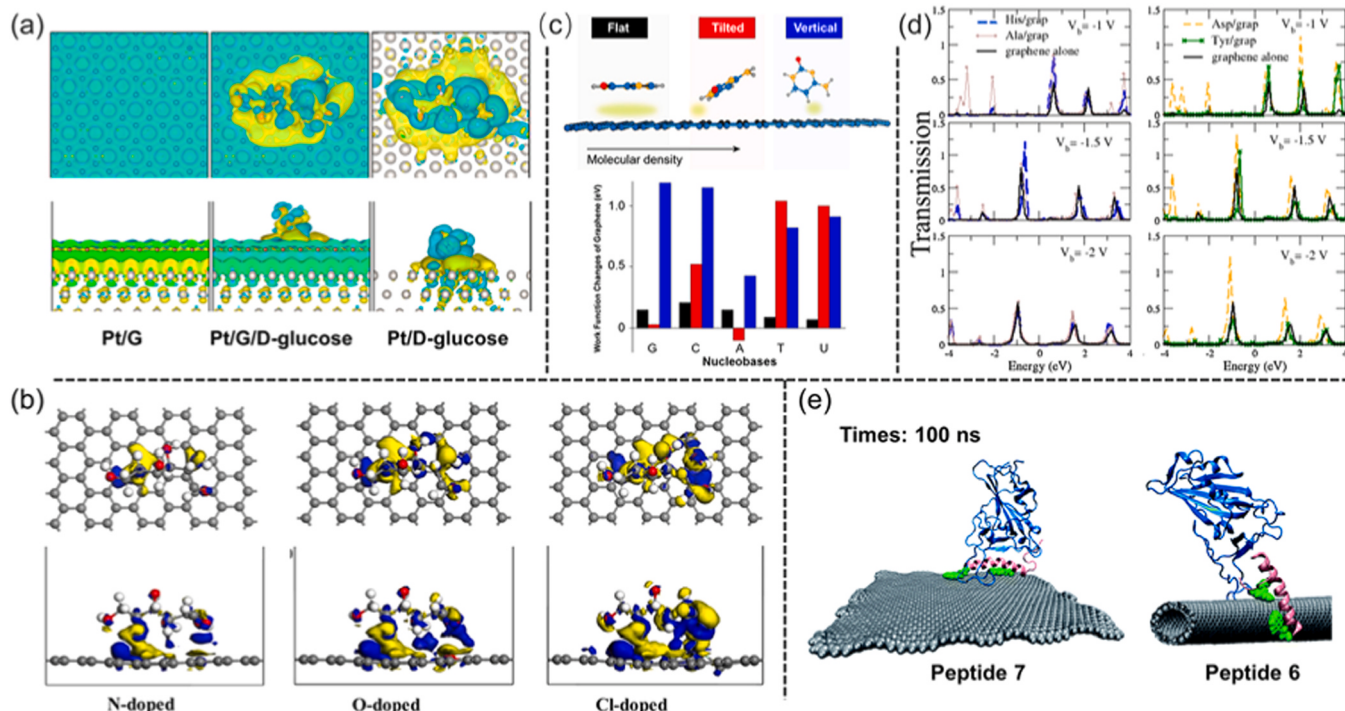


**Fig. 4.** a) The charge density differences of Pt/G, Pt/G/D-glucose, Pt/D-glucose, respectively. a) Reproduced with permission. [70] Copyright 2020, MDPI. b) Charge density differences plot of D-glucose molecules adsorbed on X-doped graphene surface. b) Reproduced with permission. [72] Copyright 2019, Elsevier. c) Work function changes of DNA/RNA nucleobases on graphene surface. c) Reproduced with permission. [73] Copyright 2017, American Chemical Society. d) Transmission of pristine graphene, His/graphene, Ala/graphene, Asp/graphene, and Tyr/graphene at  $V_b = -1$ ,  $-1.5$ , and  $2$  V. d) Reproduced with permission. [77] Copyright 2017, Elsevier. e) Peptide 7 with graphene, and peptide 6 with CNT in the final configuration after 100 ns of simulation. e) Reproduced with permission. [77] Copyright 2021, Royal Society of Chemistry.

investigated using DFT, with Perdew–Burke–Ernzerhof (PBE) of GGA. [72] For N-G, O-G, and Cl-G, the calculated adsorption energies ( $E_{\text{ads}}$ ) were  $-1.69$ ,  $-1.73$ , and  $-1.86$  eV, indicating that the D-glucose is strongly chemisorbed to the substrate. The presence of strong hybridization between the doped atom p state and G is responsible for the increased adsorption energy. The electron density differences show that this indicates electron transport from the doped graphene surface to the D-glucose (Fig. 4b).

In addition, graphene is expected to be a sensor of DNA/RNA, and nucleobases such as adenine (A), cytosine (C), guanine (G), thymine (T), and uracil (U) are deoxyribonucleic acid (DNA) and ribonucleic acid (RNA), which are among most vital biological groups in living organisms.[73] The adsorption geometry and electronic structure of graphene nucleobases are strongly influenced by the intermolecular interactions, resulting in the tilting of nucleobases on graphene at high molecular density. Due to the strong in-plane dipole moment of the nucleobases, their tilting leads to remarkable variations of the electronic properties in the entire graphene-nucleobase complex. And the electronic fingerprint of a nucleobase can be significantly enhanced if the molecular dipole of the nucleobase is appropriately maximized. Large differences in work function changes were observed for both planar and tilted configurations (up to 1 eV) of nucleobase molecules (Fig. 4c). The measured signal of DNA/RNA nucleobases adsorbed on graphene is therefore enhanced by using vertically aligned nucleobases. Based on DFT, Ti-doped graphene was designed as a biosensor for detecting thymine, and the properties of pristine graphene were also calculated for comparison.[74] Through the adsorption of thymine molecules, the gap between HOMO-LUMO values of Ti-G reduced (from 1.53 eV to 0.75 eV), thus increasing the conductivity value of graphene for signal detection. Methods based on DFT, the basis set LANL2MB used to investigate the adsorption capacity of Cadmium (Cd) doped graphene (Cd-G) on adenine, and it was found that Cd-G could be introduced as a strong adsorbent of adenine into biosensor applications.[75] Shao et al. investigated the prospect of application as nucleobase (A, C, G, T, U) sensing on Penta-graphene (PG) using DFT-PBE and found that the adsorption strength of PG was 8–44% higher than that of graphene.[76].

Inspired by the superlative performance of graphene for DNA detection, its potential for use as a protein sequencing was also evaluated. The effects of amino acids such as histidine (His), alanine (Ala), aspartate (Asp), and tyrosine (Tyr) on the electron transfer properties of graphene were investigated in combination with DFT and non-equilibrium Green's function (NEGf).[77] As the applied bias voltage ( $V_b$ ) is in the range  $-1 \text{ V} \sim -2 \text{ V}$ , the system has a greater specificity and sensitivity to amino acids (Fig. 4d). The calculated theoretical values of the currents obtained were in accordance with the experimental measurements. The results indicate that graphene can be used not only as an electrical signal biosensor for amino acids but also prominent in protein sequencing. The promising application of metal (Au/Ni/Cr)-doped graphene for protein tyrosine nitration (PTN) biosensor was demonstrated based on the PBE functional.[78] It was found that metal-doped graphene had a more stable structure than pristine graphene (the most stable conformation was Ni-graphene), suggesting that the introduction of metals makes graphene sensitive to nitrated tyrosine.

Recently, Ley et al. also found that peptide-modified functionalized graphene sheets and carbon nanotubes (CNTs) can be used as sensor materials for the detection of SARS-CoV-2.[79] MD simulations using the CHARMM36 force field screened 12 different peptides based on their potential binding affinity for the receptor-binding domain (RBD) of the viral spiny protein. Considering the RMSD, secondary structure conformation, hydrogen bond capacity, amino acid composition, interaction energy and PMF, two peptides, peptide 6, 7, could be potential molecules for SARS-CoV-2 detection. Then further functionalization of peptide 6 and peptide 7 in CNT and graphene, respectively, was performed, and the final configuration snapshots after simulation are shown in Fig. 4e, where both peptide-functionalized carbon nanotubes

and graphene were able to bind the RBD of the spike protein.

In summary, atomistic simulations are able to reveal the microscopic interactions between biomolecules and the surface of carbon-based materials and predict their sensing properties. The electronic properties of 2D carbon-based materials exhibit different properties due to the diversity of their isomers. The design of the sensors is inspired by the changes in electronic properties brought by the detected substances to the carriers, and thus the computational conditions need to be carefully screened during the calculation process. Additionally, a balanced combination of experimental and theoretical simulations is urgently needed to successfully gain a deeper understanding of the sensing mechanism and the origin of the sensed signals, providing both micro- and macro-guidance for the design of biosensors.

#### Computational carbon-based materials for bioimaging

Graphene fluoresces when its nanoscale lateral dimensions shrink to zero dimension. These graphene quantum dots (GQDs) are valuable in bioimaging owing to their distinct structural and optoelectronic features. Using DFT and time-dependent DFT calculations, Chen et al. found that the photoluminescence of GQDs allows for modulation by their size, heteroatom substitution, defects, shape, and morphology.[80] Additionally, it has been discovered that the photoluminescence of large GQDs composed of heterogeneous hybridized carbon networks is primarily composed of rooted clusters of isolated tiny  $\text{sp}^2$  by  $\text{sp}^3$  carbons. As displayed in Fig. 5a, these GQDs (G1-G6) emit fluorescence in the size range from deep UV to near IR from 0.46 to 2.31 nm, with predicted emission wavelengths of  $\sim 235$  and  $\sim 872$  nm for the counterparts, respectively.[80] LUMO and HOMO molecular orbitals indicate the photoluminescence emission is mostly occurring in the pyrene domain, whereas HOMO is primarily from the hexamethyl-pyrene domain (Fig. 5b). Additionally, Karatay et al. investigated polyethyleneimine-functionalized N-doped GQD (PEI N-doped GQD) and its top-loaded silver nanoparticles (denoted as AgNPs/PEI N-doped GQD) composites for bioimaging applications.[81] The experiment showed that the PEI N-doped GQD at maximum 446 nm displayed a strong emission spectrum (at 356 nm excitation wavelength), while the AgNPs/PEI N-doped GQD nanocomposite showed a weak fluorescence intensity (at 344 nm excitation wavelength). The shortened excited state lifetime of AgNP/PEI N-doped GQDs compared to PEI N-doped GQDs by ultrafast transient absorption spectroscopy which was attributed to the electron transfer from PEI N-doped GQDs to AgNPs. Additionally, treatment of lung adenocarcinoma cells with both materials revealed specific fluorescent signals only in the cytoplasm of Ag/PEI N-doped GQD-treated cells. Further explaining the experimental phenomenon by DFT calculations, the HOMO-LUMO energy gap of AgNPs/PEI N-doped GQDs (1.78 eV) is smaller than that of PEI N-doped GQDs (3.10 eV) due to the interaction of the silver atoms with the hydroxyl (-OH) groups. Thus, both experimental and theoretical results point to the superior imaging ability of AgNPs/PEI N-doped GQDs over PEI N-doped GQDs, which encourages their application in bioimaging.

The inherent photoluminescence characteristics of carbon-based materials are a critical attribute accessible for biodistribution and homing in living cells. Potsi et al. found that dodecylamine (CDA) and hexamethylene diamine (CHMDA) functionalized fluorinated graphene exhibit intrinsic fluorescence. The emission properties are due to the energy gap designed by the choice of amine.[82] The bandgap of CDA (0.6 eV) and CHMDA (1.2 eV) functionalized fluorinated graphene is significantly lower compared to fluorinated graphene (3.06 eV) (Fig. 5d). This matches the experimentally measured redshift of CDA's photoluminescence emission maxima compared to CHDMA. These findings imply that functionalized photoluminescent graphite derivatives have a significant future for bioimaging applications.

The photoluminescence of carbon-based materials can be tuned by their dimensional size, edge morphology, shape, chemical functional group functionalization, heteroatom doping and defect engineering.

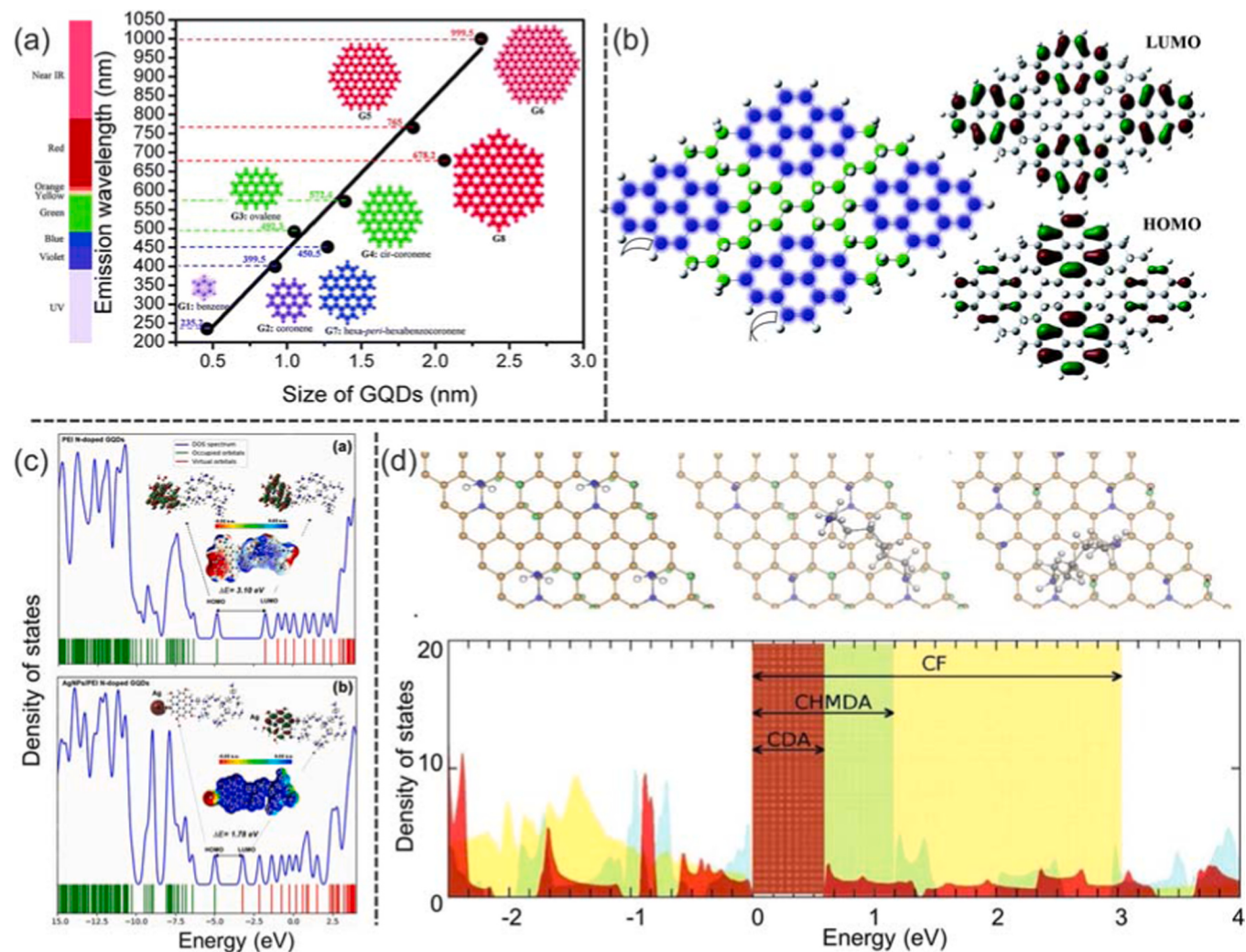


**Fig. 5.** a) Emission wavelength (nm) versus GQD diameter plot calculated by TDDFT method and b) its LUMO and HOMO schematics. a,b) Reproduced with permission.[80] Copyright 2014, Royal Society of Chemistry. c) DOS with HOMO and LUMO visualization of the PEI N-doped GQDs and AgNPs/PEI N-doped GQDs. c) Reproduced with permission.[81] Copyright 2020, Elsevier. d) Structure and DOS of amine-functionalized N-doped fluorographene, CDA and CHMDA. d) Reproduced with permission.[82] Copyright 2019, Elsevier.

DFT and TDDFT calculations are utilized to reveal the excited state nature of the fluorophores as well as the HOMO-LUMO energy gap and frontier molecular orbitals. The calculations not only provide rational theoretical guidance for the design of pre-fluorescent agents, but also provides insightful explanations for experimental observations.

#### Computational carbon-based materials for drug delivery

The invention of new and effective drug delivery systems (DDS) is an urgent bottleneck for modern medicine, which allows for precise and targeted drug delivery and improved drug efficacy. In recent years, rapid advances in nanotechnology have opened up many exciting opportunities for the treatment of disease. The discovery of graphene has sparked a flurry of research into the utility of this novel material in DDS. Carbon-based materials have great adsorption capacity, superior strength, biological compatibility, colloidal stability, and a huge surface area. Liu and colleagues revealed that functionalized oxidized graphene was biocompatible and exhibited no toxicity.[83] Despite the interest in this single-element two-dimensional material, the intrinsic and inevitable nature of the interactions between biomolecules and graphene remains unknown, hindering graphene's progress in biology.[84] MD simulations are progressively demonstrating their value in the study of biological applications, and they have the potential to significantly

increase our capacity to gather insights and precise information about biological systems and materials science.

Zhang proposed a novel drug delivery based on dense DFT, and Fe and N modified graphene (Fe-N-Graphene) performed satisfactorily in the transport of  $\beta$ -lapachone anticancer drugs.[85] The results indicated that Fe-N-Graphene exhibited large adsorption energy of 1.67–1.73 eV for  $\beta$ -lapachone molecules, which ensured drug delivery stability. The adsorption energy of  $\beta$ -lapachone was significantly reduced after protonation in acidic solution to about  $0.51 \sim 0.88$  eV, reducing charge transfer to the substrate during adsorption (Fig. 6a). This suggests that  $\beta$ -lapachone molecules are easily released from Fe-N-Graphene after reaching the acidic medium of cancer tissue. DDS of cation- $\pi$  interactions between graphene and DOX formed by the insertion of Li, Na, K, Be, and Mg were investigated.[86] The AIM and NBO analyses showed that the G-Be-DOX complex was an optimal drug carrier because it had more interatomic interactions with DOX and MD simulations confirmed its stability under biological conditions (Fig. 6b).

Utilizing DFT and MD simulations, Sa et al. computationally investigated the computational interaction of 5-fluorouracil (5-FU) anti-cancer drugs on graphene oxide surfaces (GO).[87] DFT calculations showed that the process of adsorption of 5-FU medicine on various functional groups of GO was thermodynamically stable, and 5-FU molecules could be physically adsorbed on GO. MD simulation results show

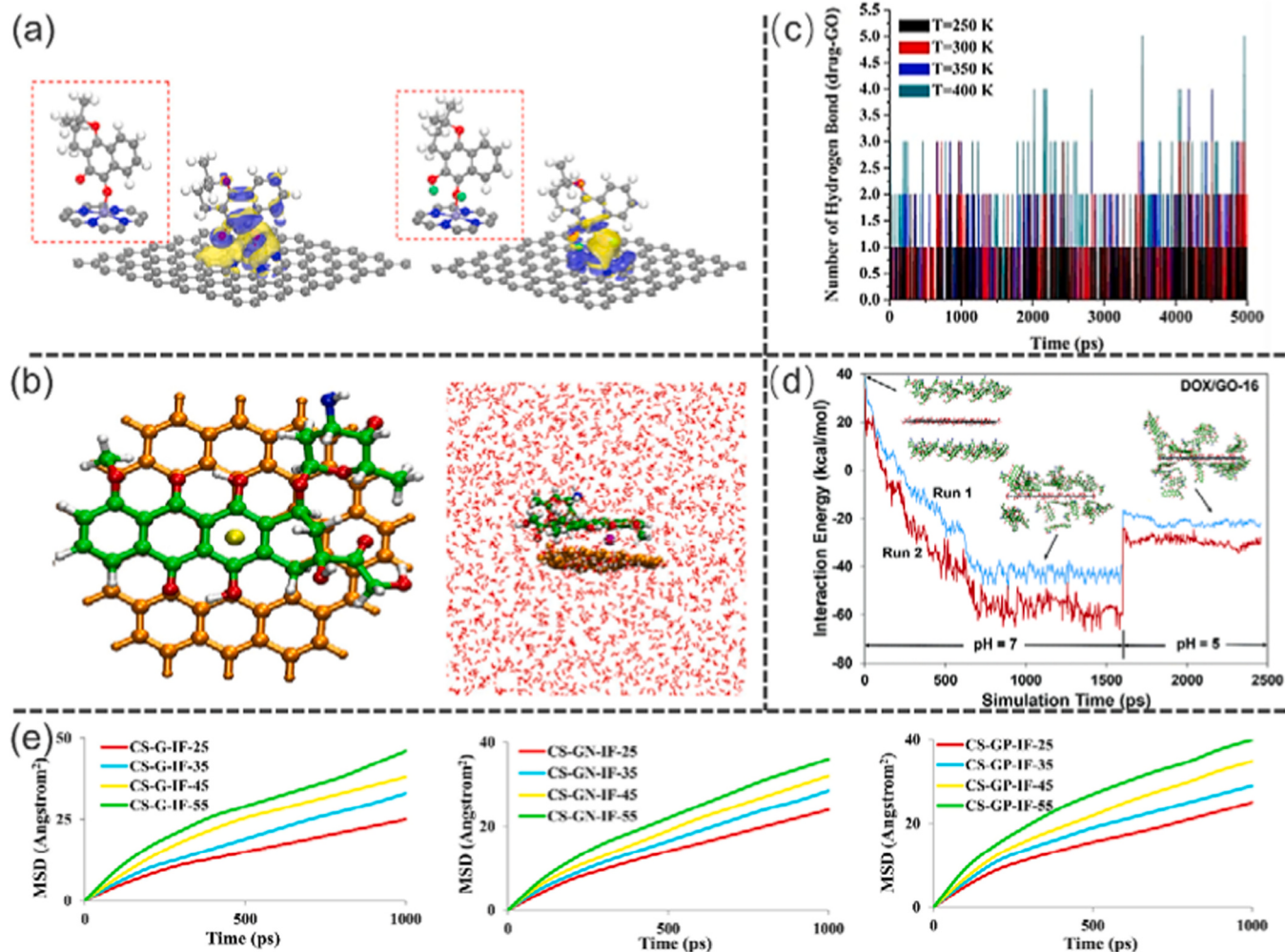


**Fig. 6.** a) The differential charge density distribution of unprotonated and protonated  $\beta$ -lap on Fe-n-graphene a) Reproduced with permission [85]. Copyright 2022, Taylor & Francis. b) Geometric model of G-Be-DOX and the model after MD simulation. b) Reproduced with permission [86]. Copyright 2022, Elsevier. c) The number of hydrogen bonds between drug and the surface of GONS. c) Reproduced with permission [87]. Copyright 2017, Springer. d) MD simulation plots of loading and releasing DOX on GO-16 at pH 7 and 5, respectively. d) Reproduced with permission [88]. Copyright 2016, Royal Society of Chemistry. e) Mean square displacement plots of IF diffusion for the CS-G-IF, CS-GN-IF and CS-GP-IF composite systems. e) Reproduced with permission [92]. Copyright 2019, Elsevier.

that hydrogen bonding (HB) interactions dominate among 5-FU molecules and intrinsic functional groups of GO, and are also important to ensure the most stable 5-FU/GO structure (Fig. 6c). Additionally, by raising the temperature from 250 K to 400 K, 5-FU medicine is strongly adsorption on the GO surface, as evidenced by the greatest negative van der Waals interaction energy and numerous hydrogen bonds between GO and drug molecules. The combined influence of graphene oxide oxygen-containing functional group concentration and pH on drug-carrier interactions has been neglected to a large extent. Applying neutral, acidic, and basic pH levels, Mahdavi and co-workers researched the interaction of DOX on pure graphene (PG) and GO [88]. In general, the amount of adsorbed DOX expands with the rise of oxygen concentration on the GO surface. The interaction energy of the DOX/GO-16 (O/C ratio 1:6) system increased by  $\sim 23$  kcal mol<sup>-1</sup> on average when the pH was reduced to 5, indicating a more relaxed attachment of DOX to the surface (see Fig. 6d). They recombine to generate a more vertical structure on the surface, indicating that DOX was more easily released at acidic pH levels. Typically, fluorinated graphene oxide (FGO) functionalized with amino polyethylene glycol (PEG) pre-linked with folic acid (FA) (FGO-PEG-FA) enables the preparation of novel nanocarriers. [89] The anticancer drugs doxorubicin (DOX) and camptothecin (CPT) were efficiently loaded onto FGO-PEG-FA individually or together in a precise mixing ratio. Specifically, DOX loading increased linearly with

increasing concentration, but CPT loading was almost constant ( $\sim 10.5\%$ ). The drug-FGO-PEG-FA interactions were subjected to detailed DFT calculations, i.e., the simultaneous loading of DOX and CPT onto the surface of FGO-PEG-FA resulted in not only vdW interactions, but also the formation of significant hydrogen bonds. The introduction of fluorine atoms provided more active sites for intermolecular interactions between the drug and FGO compared to GO. Similarly, the interaction of the anticancer drugs 5-Fu and pyrazinamide (PZA) on CN and FA-functionalized CN nanosheets (FA-CN) was intensively analyzed by DFT and MD simulations. [90] DFT results showed the presence of strong HBs between the drugs and FA-CN. RDF results demonstrated better adsorption of drug molecules on FA-CN nanosheets and closer to the carrier. MSD results revealed that folic acid affects the drug movement and reduces its diffusion coefficient. FA-CN nanocarriers are good candidates for anticancer drug delivery.

Graphene surface modified with folic acid (FA-G) can be used as a carrier to carry DOX and camptothecin (CPT) as dual drug delivery material. [91] DFT and MD simulation findings showed that the drug molecules voluntarily moved to the carrier and generated stable compounds. In raw graphene-based structures, drug molecules develop robust  $\pi$ - $\pi$  interactions with the support surface. FA-G allows for improved targeting and also enhances drug carrier interactions. DOX molecules interacted stronger with graphene and FA-G than with CPT.

The improvement of biocompatibility of carbon-based materials in biomedical applications is pressing and usually requires the preparation of various functionalized materials. Chitosan (CS) is the carrier material of choice because of its bioavailability, adhesiveness, biocompatibility, toxicity-free, antibacterial, and immune-enhancing properties. Chitosan was able to be complexed with nanoparticles containing graphene (G), n-doped graphene (GN), or p-doped graphene (GP), and the delivery capacity of the anticancer drug ifosfamide (IF) was probed by the MD method to compare which complex is the optimal drug-carrying material.<sup>[92]</sup> The free volume (FV) and fractional free volume (FFV) rise with increasing temperature (from 298.15 K to 328.15 K), and CS-GN-IF was discovered to be the preferred DDS with the smallest IF diffusion coefficient (Fig. 6e).

The computational tool provides a good description of the interaction between drug molecules and carbon-based materials, the formation of hydrogen bonds, drug molecule delivery pathways, and the associated thermodynamics and kinetics. Moreover, MD simulation provides an effective simulation of the weakly acidic environment in the vicinity of tumors, which enables drug delivery calculations to be close to the real biological environment.

### Computational carbon-based materials as Nanozyme

Because of their superior stability and robustness, adjustable activity, and lower production costs, nanomaterials with enzyme-like characteristics (nanozymes) can be regarded as effective substitutes for real enzymes.<sup>[93]</sup> A variety of nanozymes, mainly including members of the oxidoreductase family such as peroxidase (POD), catalase (CAT), cytochrome C oxidases (OD), and superoxide dismutase (SOD). Two-dimensional (2D) materials have a huge surface area and can be exploited as possible catalytic active sites for nanozymes in a variety of interesting applications. However, the investigation of the fundamental microscopic processes and dynamics of nanozymes is still challenging. DFT calculations play a critical role in exploring the mechanisms and kinetics of nanozymes. These calculations either anticipate the microscopic information of the catalytic process or lead to the development of theoretical models that characterize the physicochemical regulations.

With regard to its metal-free features, high stability, and outstanding biocompatibility, the graphene category of nanomaterials, which includes graphene, graphene oxide (GO),<sup>[94,95]</sup> reduced graphene oxide (rGO)<sup>[96]</sup>, and graphene quantum dots (GQDs),<sup>[97]</sup> has been employed

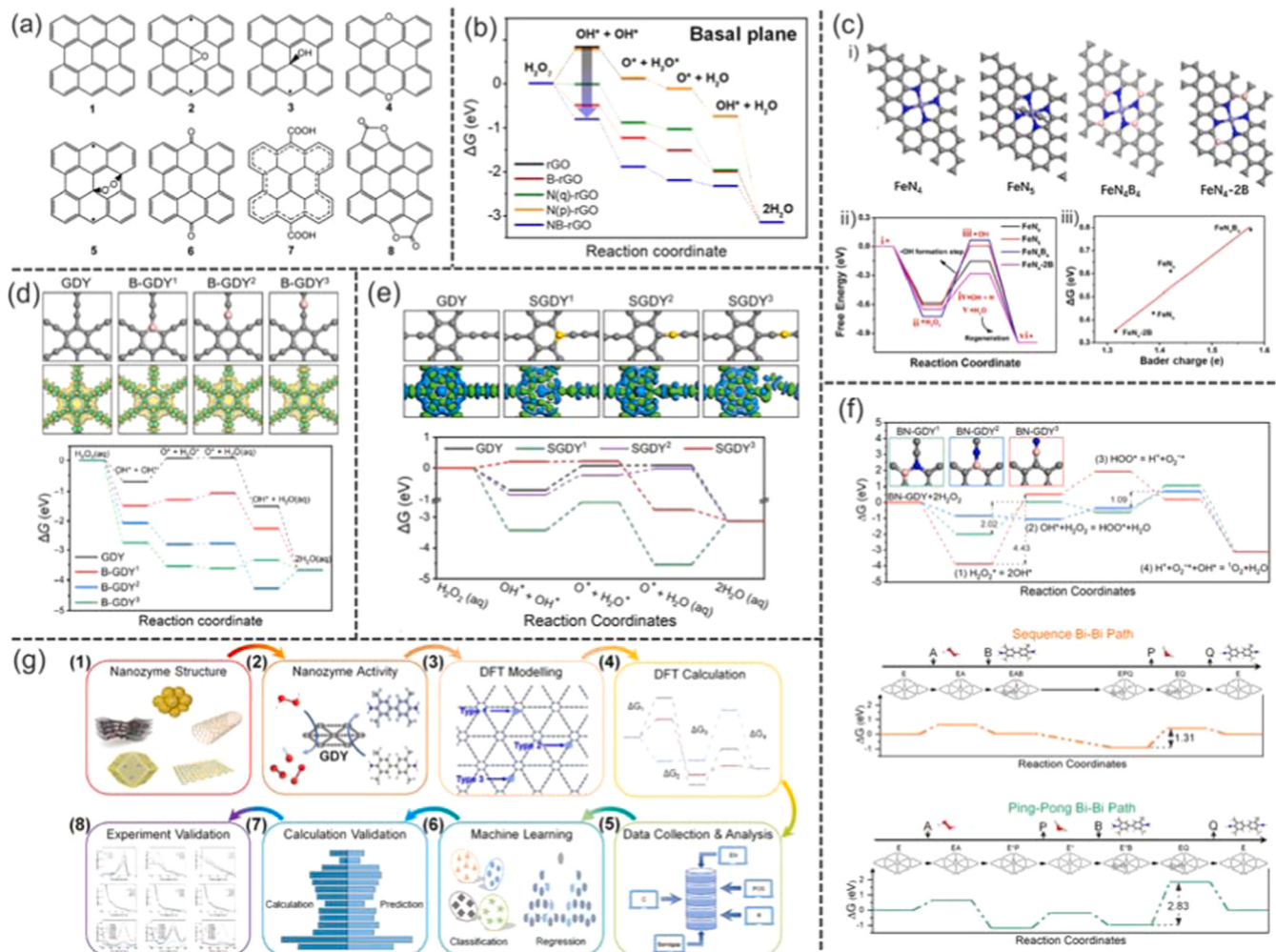


**Fig. 7.** a) Geometries of pristine graphene (1) and GO with different functional groups (2–8). a) Reproduced with permission.<sup>[98]</sup> Copyright 2020, Royal Society of Chemistry. b) Free energy curves of rGO, B-rGO, N(q)-rGO, N(p)-rGO and NB-rGO. b) Reproduced with permission.<sup>[100]</sup> Copyright 2022, American Chemical Society. c) i) FeBNC SAzymes with different structures, ii) their free energy diagrams for  $\text{H}_2\text{O}_2$  reduction and iii) the energy barrier relationship between the iron atoms in the structures and OH charge formation. c) Reproduced with permission.<sup>[102]</sup> Copyright 2020, Elsevier. Geometric model, electric differential density and reaction Gibbs free energy diagram of d) B-GDY and e) SGDY. d) Reproduced with permission.<sup>[104]</sup> Copyright 2022, Springer nature. e) Reproduced with permission.<sup>[101]</sup> Copyright 2022, Elsevier. f) Gibbs free energy diagrams of BN-GDY peroxidase-like reactions and chemical transformations of different pathways. Reproduced with permission.<sup>[105]</sup> Copyright 2022, American Chemical Society. g) Schematic diagram of the process of ML-assisted screening based on GDY-based nanozymes. Reproduced with permission.<sup>[111]</sup> Copyright 2022, American Chemical Society.

in nanozymes. GO and rGO can produce hydroxyl radicals with high oxidative properties by activating  $\text{H}_2\text{O}_2$ , exhibiting peroxidase-like POD activity. Although GO and rGO include a range of functional groups that contain oxygen, such as epoxy, hydroxyl, ethers, endoperoxides, carbonyl, carboxyl, and esters (Fig. 7a), the active center and the fundamental mechanism of peroxidase mimetic activity are unidentified. To confirm the POD activity center of GO, the possible catalytic mechanism was explored by DFT calculations.<sup>[98]</sup> The activation of the C=O bond is a critical factor in the catalytic process, and this finding promotes the improvement of the carbon-based nanzyme activity.

Heteroatom doping has been proposed as a viable technique for altering the inherent characteristics of carbon-based materials. In a recent study, N doping onto rGO was demonstrated to significantly increase POD activity.<sup>[99]</sup> DFT investigations revealed that the lone pair of electrons carried by N-pyrene promoted the stable generation of radical oxygen on the surface of rGO, resulting in effective tetramethylbenzidine (TMB) oxidation. N and B co-doped rGO (NB-rGO) were developed as carbon-based materials peroxidase-mimicking with much higher catalytic activity than classical mimetic peroxidase carbon-based nanozymes.<sup>[100]</sup> DFT analysis showed that the increased peroxidase activity of NB-rGO upon successive doping of N and B is attributable to the modification of the active site on graphene by the dopant. Interestingly, the peroxidase activity of the B atom is retained while the inert N atom is transformed to a catalytically activated center co-doped with N and B atoms (Fig. 7b). Moreover, the adsorption of OH\* on the B atom close to the pyridine N atom becomes greater than in any other position ( $\Delta G_{\text{OH}^*+\text{OH}^*} = -0.81 \text{ eV}$ ). In summary, the combined effect of N and B co-doping improves peroxidase activity further when contrasted with nondoped or monodoped (N or B) graphene. In addition, Kim et al. found that the Fe- and N-coexisting rGO (Fe-N<sub>4</sub>-rGO) is much more active than the monodoping rGO with Fe- or N- (Fe-rGO or N-rGO).<sup>[101]</sup> The O\* + H<sub>2</sub>O\* production step in Fe-N<sub>4</sub>-rGO exhibits the greatest activity (i.e., with a reaction energy  $-0.99 \text{ eV}$ ) of all the materials investigated. The effect of the kind of central metal atom in the nitrogen-ligated rGO on activity was further investigated by substituting Fe with Co (Co-N<sub>4</sub>-rGO) or Ni (Ni-N<sub>4</sub>-rGO), and the energy required for the O<sub>2</sub> dissociation reaction was calculated. According to the DFT results, Fe-N<sub>4</sub>-rGO has the highest catalytic activity and excellent selectivity.

In addition to the typical FeN<sub>4</sub> nanzyme active site, B-doped FeN<sub>4</sub> nanzyme likewise exhibit excellent enzyme catalytic activity.<sup>[102]</sup> Aberration corrected high-angle annular dark-field scanning transmission electron microscopy (AC-HADDF-STEM) and X-ray absorption near-edge structure (XANES) confirmed the successful synthesis of B-doped FeN<sub>4</sub> single-atom nanozymes (SAzymes). The enhanced activities of FeBNC SAzymes were compared with FeNC. The catalytic activities of POD, OD, CAT, and SOD were increased by 191.2%, 72.5%, 11.9%, and 5.3%, respectively, demonstrating that B doping selectively enhances the POD-like activity of Fe-NC SAzyme. Based on theoretical calculations, the free energies of H<sub>2</sub>O<sub>2</sub> on FeN<sub>4</sub>, FeN<sub>5</sub>, FeN<sub>4</sub>B<sub>4</sub>, and FeN<sub>4</sub>B<sub>2</sub> (Fig. 7c, i) nanozymes were found to have the lowest reaction energy barriers for FeN<sub>4</sub>B<sub>2</sub>, which is consistent with experimental observations (Fig. 7c, ii). It is noteworthy that the nanozymes with larger coordination numbers (FeN<sub>4</sub>B<sub>4</sub>) are detrimental to the catalytic cycle because they weaken the adsorption of -OH, resulting in a larger energy barrier for -OH formation, which is not favorable for catalysis. More importantly, the energy potential correlates almost linearly with the positive charge of the central iron atom (Fig. 7c, iii).

Graphdiyne (GDY) is a novel 2D carbon nanomaterial consisting of 18 carbon atoms with a highly  $\pi$ -conjugated structure, which has been shown to have excellent nanzyme activity in recent years.<sup>[103]</sup> Heteroatoms were employed to dope GDY in order to boost its catalytic activity by producing a greater number of defect sites. Bi et al. constructed boron doped graphdiyne nanosheets (B-GDY) to simulate the performance of (POD).<sup>[104]</sup> The electron density difference suggests that with boron doping at different places in B-GDY (Fig. 7d, top), and B

acts as the active center of the reaction owing to the differential electronegativity of the B and C atoms. From the variation of  $\Delta G$  (Fig. 7d, bottom), B-GDY<sup>3</sup> ( $\Delta G_{\text{OH}^*+\text{OH}^*} = -2.75 \text{ eV}$ ) is a thermodynamically favorable site for the production of both adsorbed OH\* compared to B-GDY<sup>1</sup> ( $-1.48 \text{ eV}$ ) and B-GDY<sup>2</sup> ( $-2.0 \text{ eV}$ ). Thus, the addition of boron heteroatoms to B-GDY could increase the number of catalytically active sites and thus promote the pod-like activity of B-GDY. Very similarly, Zhang et al. demonstrated that sulfur-doped graphdiyne (SGDY) also enhanced POD activity. The production of O\* and H<sub>2</sub>O\* is the rate determining step in the reaction rate with  $\Delta G$  of 0.92 eV and 0.60 eV, respectively, indicating sluggish catalysis. For SGDY<sup>3</sup>, the rate determining step HO\* formation and  $\Delta G$  is only 0.02 eV (Fig. 7e). In comparison to other analogues, SGDY<sup>3</sup> may effectively lower the energy barrier and boost peroxidase-like activity. In the case of SGDY<sup>3</sup>, the electrons of the sulfur atom protrusion from the substrate, which could help in lowering the energy barrier and putting it in the active center of the catalytic process. B, N co-doped GDY was also studied,<sup>[105]</sup> with BN-GDY<sup>2</sup> maintaining the minimal reaction energy (1.04 eV for BN-GDY<sup>1</sup>, 0.73 eV for BN-GDY<sup>2</sup>, and 1.92 eV for BN-GDY<sup>3</sup>), suggesting a higher active site for BN-GDY<sup>2</sup> (Fig. 7f). More importantly, the chemical conversion of the entire peroxidase simulation process was also studied, and DFT calculations were performed for the ping-pong Bi-Bi pathway and the sequence Bi-Bi pathway of BN-GDY<sup>2</sup>.<sup>[106]</sup> According to the findings, the sequence Bi-Bi pathway is the primary dynamic mechanism of the peroxidase simulation process.

Machine learning (ML), as a branch of artificial intelligence, has been successfully applied as a processing-efficient and versatile powerful tool. Because it can objectively explain massive data sets in various fields, it can accurately predict and speed up the research process with realistic scientific research. In recent years, machine learning has been widely used to predict the structure-activity relationship of nanozymes.<sup>[107–110]</sup> Zhu et al. conducted machine learning on non-metal atom-doped GDY as a POD reaction, combined with DFT and experiments to screen out two types of GDY (B- and N-doped) with excellent performance, and the research steps are shown in Fig. 7g.<sup>[111]</sup> Using the ML algorithm (Extreme Gradient Boosting, XGB) to predict the maximum energy barrier ( $R^2 > 78\%$ ) or maximum energy consumption step size (accuracy > 65%) of various non-metal-doped GDYs based on part of the calculation data, effectively reducing calculated cost. Furthermore, the experimental results show that the activity order of non-metal atom-doped GDYs with H<sub>2</sub>O<sub>2</sub> as substrate is N > Si > B > O > S > P, and these trends are consistent with the predictions. Therefore, ML is a powerful tool to assist in the screening of DFT computational structures, and can be used as a reference guide for experimental guidance.

Problems of nanozymes made of carbon-based materials still remain to be solved, such as active site-structure relationship, catalytic mechanism, and activity-selectivity balance. Computation provides a comprehensive prediction of the changes in geometry and energy during the reaction process, so that the mechanism of action of the catalytic activity of nanozymes is revealed by the computational microscopic mechanism. However, the current nanoscale computations mainly predict the microscopic details of the catalytic process to complement the experiments, and there is still a lack of a "gold standard" to guide the autonomous design of nanozymes. The utilization of machine learning to intelligently design nanozymes models and optimize their application provides valuable guidance for the development of a new generation of nanozymes.

## Advances in the calculation of h-BN for bioapplications

### Structure and electronic properties of h-BN

BN is isomorphic with carbon (C) and exists in various crystalline forms. Hexagonal (h-BN) is a white, smooth BN polycrystalline form with a graphite-like layered structure, also known as white graphite. The

structure is formed by the intercalation of B and N atoms through van der Waals interactions to form a 2D flat layer. The *h*-BN is made up of  $sp^2$  hybridized, extremely covalent, and highly polarized BN bonds organized in a graphene-like sheet structure.[112] However, unlike graphene, BN is highly polarized containing electronegative N atoms, which may result in anisotropic characteristics and it is also an insulating wide bandgap ( $\sim 5.2$  eV) material.[113] Monolayer *h*-BN sheets are extremely promising as materials for biological applications as *h*-BN has superior chemical stability to monolayer graphene by virtue of its high chemical stability and minimal toxicity.

### Theoretical investigation of *h*-BN in bioapplications

#### Computational *h*-BN as biosensor

The pattern of interaction of nucleobases and *h*-BN is found to differ in comparison with that of graphene. *h*-BN sheets are polar materials exhibiting the non-uniform distribution of charges and polarization anisotropy, and the surface polarization greatly influences the adsorbate's detailed orientation and behavior.[114] With its strong fluorescence burst capability and sensitivity for DNA/RNA, the *h*-BN sheet may be employed as a sensor platform for swift detection. Utilizing the absorption and emission properties of the nucleobases of Al atom-doped *h*-BN (Al<sub>x</sub>hBN) on the theoretical energy level M062X/6-31 G\*, the stability of the nucleobases on the calculated Al<sub>x</sub>hBN sheet has a C > G > A > T trend.[115] The NCI, DOS and AIM analyses indicate nucleobases adsorb physically on *h*-BN layers with electrostatic interactions, and the influence of aluminum doping on *h*-BN sheets affects base

adsorption and optical characteristics. For the purpose of monitoring the sequence-specific adsorption of bases on such sheets, thymine- and guanine-tagged fluorophores complexed with *h*-BN sheets and Al<sub>x</sub>hBN films, respectively, displayed a large redshift (55 nm) in their emission spectra and a large blue shift (43 nm) (Fig. 8a). Another potential biosensor was the isomer of haeck-BN, which consists of square and octagonal rings producing a planar haeckelite structure (Fig. 8b).[116] Using Grimme dispersion-corrected DFT, the magnitude of the adsorption energy of nucleobases on haeck-BN was calculated to determine the strength of their adsorption in the order of G > T > A > C > U. Haeck-BN is expected to have an ultra-fast recovery time (in milliseconds) for nucleobases, especially 0.6 ms for U and 120 ms (C), 130 ms (A) and 292 ms (G) for other nucleobases, respectively, to evaluate its potential as a nucleobase biosensor. Furthermore, *h*-BN can also be structurally modified to improve biosensitivity by compounding with graphene to form two-dimensional hybrid nanosheets, where the dipole moment interactions of the material control the orientation of the nucleobases.[117] Rani et al. used DFT and NEGF based calculations to graphene/*h*-BN heterostructures made of devices that use single electron transistor (SET) and have high resolution, energy-efficient design, and low manufacturing costs may identify and sequence different DNA/RNA nucleobases (Fig. 8c).[118]

In living organisms, nucleobases usually occur in pairs and are connected by hydrogen bonds; therefore, it is necessary to explore the interactions between nucleobase pairs and substrates. Ding et al. investigated the interaction between nucleobase pairs and *h*-BN by DFT and MD calculations.[119] Eight types of hydrogen-bonded nucleobase

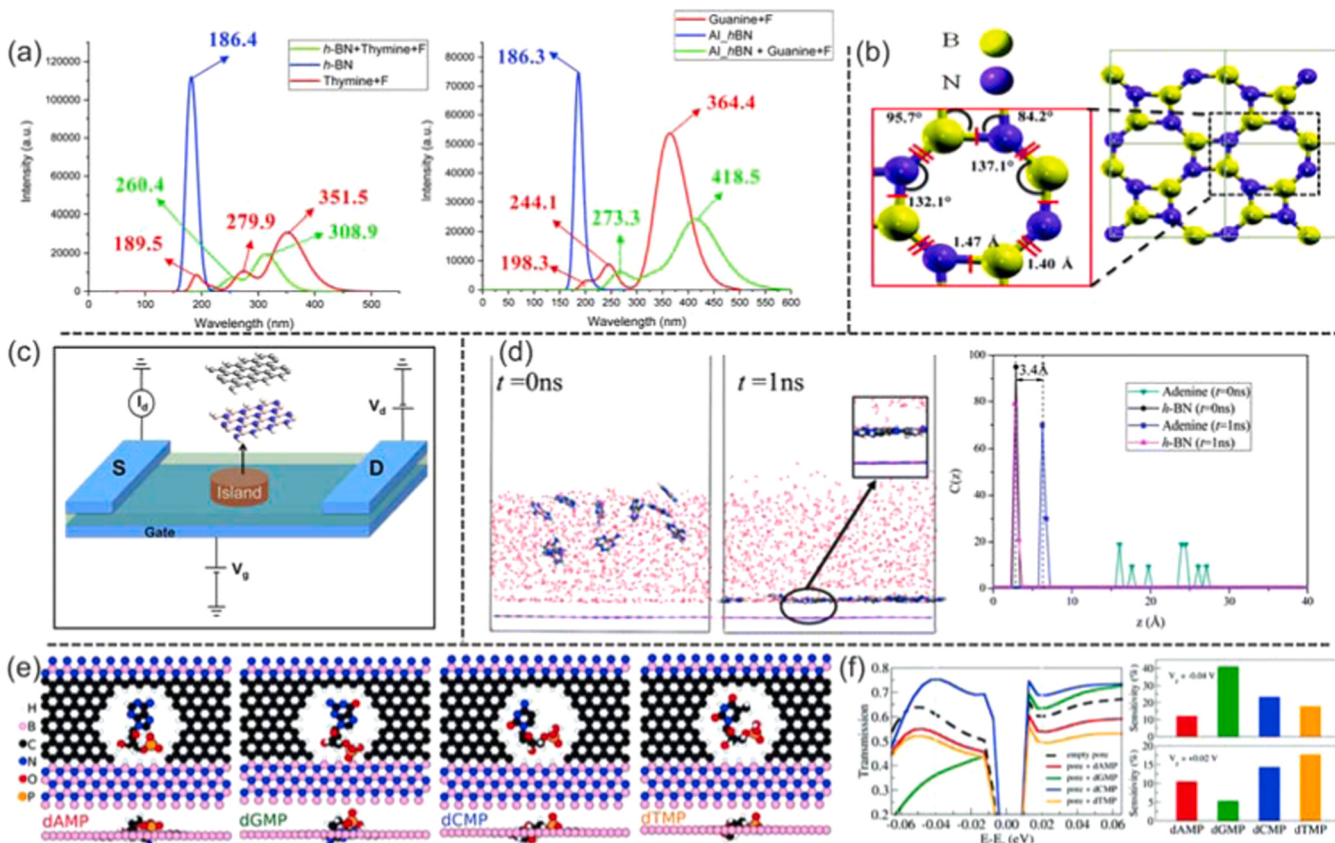


**Fig. 8.** a) Absorption spectra of nucleobases, *h*-BN and their complexes. a) Reproduced with permission.[115] Copyright 2022, Royal Society of Chemistry. b) Optimized structure of haек-BN. b) Reproduced with permission.[116] Copyright 2018, Royal Society of Chemistry. c) Schematic diagram of the graphene/*h*-BN-based SET device. c) Reproduced with permission.[118] Copyright 2021, Elsevier. d) Configuration snapshot of adenine and *h*-BN system at  $t = 0$  ns and  $t = 1$  ns (left) and concentration distribution of centroid (right). d) Reproduced with permission.[119] Copyright 2013, Royal Society of Chemistry. e, f) Optimized structure, zero-bias transmission spectrum and sensitivity of dAMP, dGMP, dCMP and dTMP on *h*-BN/G. e, f) Reproduced with permission.[121] Copyright 2017, Royal Society of Chemistry.

pairs, including three types of Watson-Crick pairs [120] (AT, GC, and AU) and five non-Watson-Crick pairs (GG, AA, TT, CC, and UU), and their selection of the corresponding stacked forms as adsorbates were used. It is shown that physical adsorption and interconnection facilitate hydrogen bonding interactions in both gas and aqueous phases on the *h*-BN surface. By MD simulations, the nucleobase rose from the initially predicted 20 Å on the BN surface to 3.4 Å after 1 ns, demonstrating that *h*-BN is a sensitive nucleobase pair sensor in the aqueous environment (Fig. 8d).

Souza et al. found that graphene sheets embedded in hexagonal boron nitride (*h*-BN) sheets (*h*-BN/G) and fabricated nanopores structures applied to detect DNA nucleotides. [121] The four nucleotides are deoxyadenosine monophosphate (dAMP), deoxyguanosine monophosphate (dGMP), deoxycytidine monophosphate (dCMP) and deoxythymidine (dTTP), and their relaxed structures on *h*-BN/G are shown in Fig. 8e. Energy-resolved transmission spectroscopy studies show that adsorption of DNA nucleotides on the material relative to the original *h*-BN/G can bring about significant transmittance changes (Fig. 8f, left). Interestingly, sensors based on the *h*-BN/G design require only a single gate voltage to distinguish between DNA nucleotides with sensitivity differences greater than 5% (Fig. 8f, right). Recently, they found that homogeneous material (*h*-BN/G)-based sensors can also be used to detect and differentiate nucleobases, which provides direction for fast, sensitive, and low-cost DNA sequencing. [122].

A comprehensive insight into the factors affecting the performance of *h*-BN as a potential biosensor, such as surface defects, introduction of heterogeneous structures, and heteroatom doping, is presented based on theoretical models. However, the electronic and magnetic properties of *h*-BN change in the presence of defects. [123] These changes are worth examining, as defect sites are usually more reactive and thus may have higher sensing performance. This phenomenon has apparently been noticed by few researchers, which requires that subsequent computational studies need to employ high-precision exchange-correlation functionals and incorporate dispersion corrections to determine the changes due to defects in order to obtain accurate computational results.

#### Computational *h*-BN for drug delivery

*h*-BN is a strong contender for drug delivery since it is not only non-toxic to people but also has special qualities including chemical inertness, surface tunability, and structural stability. The delivery performance of *h*-BN and functionalized *h*-BN with polyethylene glycol (PEG-*h*-BN) for the anticancer drug gemcitabine (Gem) was investigated. [124] The drug "π-π" stacked on *h*-BN, according to DFT calculations, but the strong HBs stabilized the "π-π" layer of PEG-*h*-BN, which enhanced the adsorption energy by about 20%. The type of interaction between drug and carrier molecules was determined by reduction density gradient (RDG) and it was found that HB formation of PEG-*h*-BN resulted

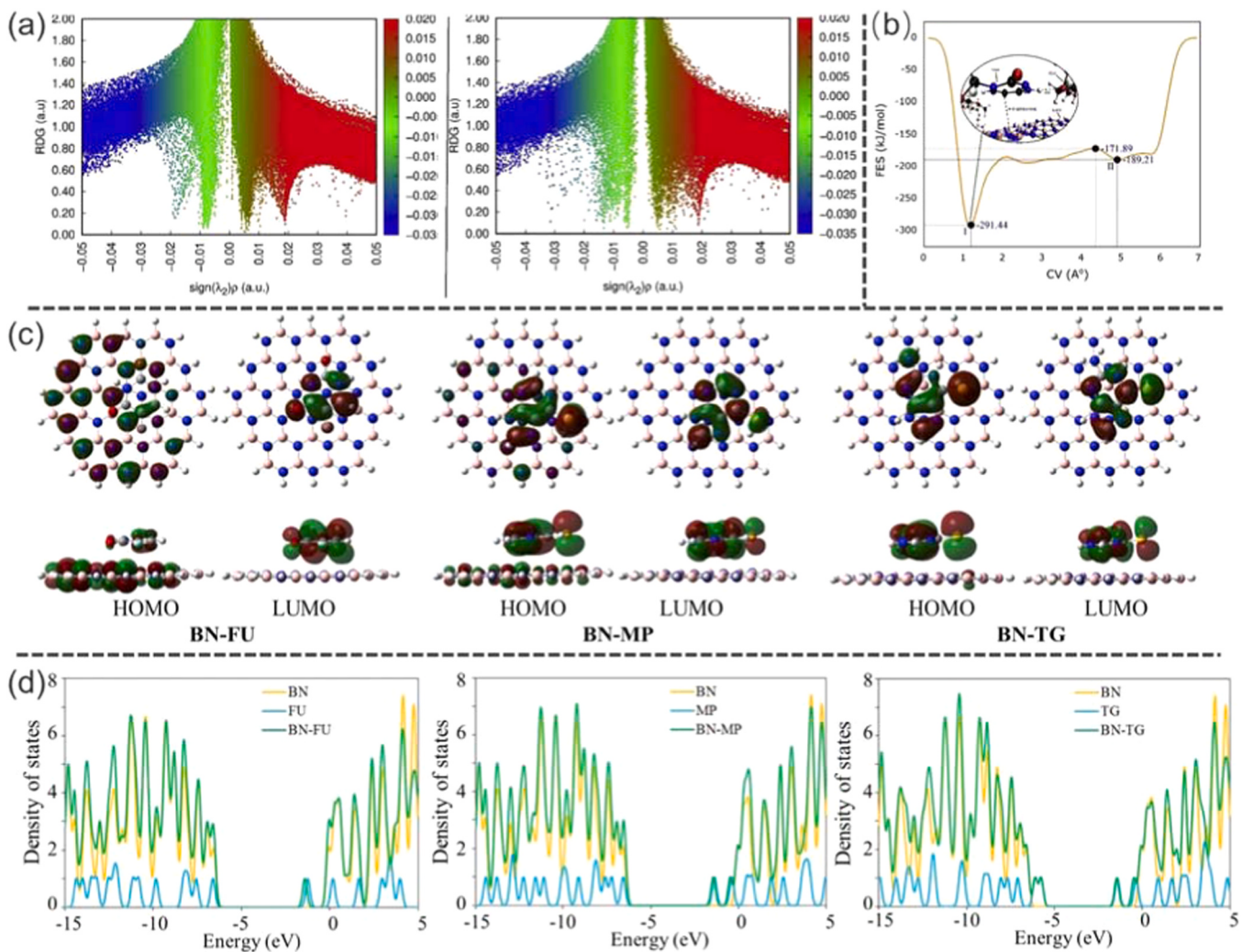


**Fig. 9.** a) Green, red and blue regions refer to van der Waals interactions, and strongly attractive interactions, respectively. b) The free energy profile of adsorption of Gem on the PEG-*h*-BN surface as a function of the center of mass of the Gem from the carriers. a, b) Reproduced with permission. [124] Copyright 2020, Elsevier. c) HOMO and LUMO orbitals and d) DOS of BN nanosheet complexes with FU, MP and TG. c, d) Reproduced with permission. [132] Copyright 2019, Elsevier.

in an addition of blue areas (Fig. 9a). Free energy calculations can provide different insights into biological systems as a theoretical computational study. However, it is not feasible to generate accurate free energy surface (FES) by running these simulations on a controlled time scale. The findings of classical MD simulations are only significant for long duration simulations.[125,126] Several methods to enhance configuration sampling have been reported.[127–130] Among them, the well-tempered metadynamics simulations are one of the successful methods to solve the free energy of a long-time process.[131] According to the metadynamics findings, the FES of the Gem/PEG-*h*-BN interface FES exhibits a global minimum at 1.2 Å, which could be connected to the development of  $\pi$ - $\pi$  stacking and HB interactions (Fig. 9b).

The interactions of the anticancer drugs 5-fluorouracil (5-FU), 6-mercaptopurine (MP), and 6-thioguanine (TG) with *h*-BN nanosheets acting as carrier platforms were studied.[132] Simulation calculations showed that the drug was hexagonally nitrogenated Adsorption on boron supports is spontaneous and exothermic. The FMO energy gap of *h*-BN nanosheets also narrowed following drug loading, according to analyses of orbital energy and density of states (Fig. 9c,d). Quantum molecular analysis of the loaded *h*-BN nanocarriers concurrently revealed higher chemical reactivity. In this context, EDA and QTAIM analysis revealed increased *h*-BN chemical reactivity following drug adsorption. Moreover, it is known by the MD method that the drug can be transported into the expected cancer cells at acidic pH because its measured interaction energy values are lower (absolute) at acidic pH than neutral environment.

Among the many surface modification methods, heteroatom doping is an important means to adjust the electronic structure. The loading process of drug 5-FU on pristine *h*-BN and *h*-BN with doping of Al, Ga, P, and As was clarified by the DFT approach employing B3LYP-D3(BJ)/6-31 g\*. [133] The physisorption properties of 5-FU in pristine, P- and As-doped *h*-BN, in contrast to the chemisorption of 5-FU in Al- and Ga-doped *h*-BN. NBO and QTAIM analysis also showed that O2(5-FU)...Al or BN(Ga) interactions of the Lewis acid-base type were the strongest interactions in these cases, forming Lewis acid-base pairs. All *h*-BN systems loaded with 5-FU are soluble and stabilized in an aqueous environment, as confirmed by their negative solubility energy. Similarly, the drug-loading properties of indomethacin (INDO) on *h*-BN functionalized with heteroatoms (Al, Ga, C, Si, P, and Cl) was studied with the same functional.[134] The calculated results show that INDO is only slightly adsorbed on pure *h*-BN, while the doping of Al, Ga, C, and Si increases the adsorption energy, thus improving the adsorption performance of INDO by *h*-BN. The conductivity of BN increases exponentially with decreasing energy gap due to the fact that the effective band gap of INDO/doped *h*-BN is narrower than that of pure *h*-BN. Combining the results of adsorption energy and electronic properties, Si is considered to be the most effective doping atom for *h*-BN as a sensor material.

Based on the previous discussion, the DFT method is investigated in detail on the nanoscale of the system, which includes processes such as bonding interactions of drug molecules, electronically excited states, and charge transfer. MD simulations are used to gain insight into the *h*-BN and drug diffusion properties in biological environments giving a detailed explanation. Well-tempered metadynamics were applied to derive the free energy surface changes of drug molecules adsorbed on the *h*-BN nanosheets. The combination of DFT, MD, and metadynamics simulations methods provides a powerful predictive tool for *h*-BN as a drug delivery.

### Advances in the calculation of transition metal dichalcogenides (TMDCs) for bioapplications

#### Structure and electronic properties of TMDCs

The bandgap modification of TMDCs allows flexible switching of metal semiconductor properties compared to graphene (zero bandgap) and 2D oxides (wide bandgap), making them sensitive and selective in

terms of biosensing efficiency. Furthermore, it is a potential nanomaterial for the creation of electrochemical and biological nano-biosensors due to its intriguing form and size.[135–137].

#### Theoretical investigation of TMDCs in bioapplications

##### Computational TMDCs as biosensor

*MoS*<sub>2</sub> is a semiconductor TMDC with an indirect band gap of 1.29 eV in its bulk form and a direct band gap of ~1.9 eV in its monolayer form. [138] The introduction of heteroatoms can modulate the local gap state of electronic properties and improve the sensitivity of the adsorbate. [139] Yang and colleagues investigated the potential of non-metallic element (Si, P, Cl, Se)-doped *MoS*<sub>2</sub> monolayers as materials for DNA/RNA sequencing.[140] The nucleobases in Si-*MoS*<sub>2</sub> have significant charge transfer (0.25 e ~ 0.36 e) and relatively strong adsorption (~3.16 ~ -2.43 eV), and the nucleobases tend to be perpendicular to the surface during structure optimization, which suggests chemisorption between them. In contrast, the nucleobases are physisorbed on P-*MoS*<sub>2</sub> for an energy range of -1.17 ~ -0.71 eV and a charge transfer range of 0.13 ~ 0.34 e (Fig. 10a). The change in the conductivity of P-*MoS*<sub>2</sub> upon absorption of individual nucleobase molecules indicates its discriminability and sensitivity to nucleobases. The expected recovery times of P-*MoS*<sub>2</sub> for the nucleobases at 400 K were 0.09 ms (U), 5 ms (T), 300 ms (A), 9 s (C), and 49 s (G). Lei et al. found that the addition of Mn can redox cycle the oxidation of DA and remarkable improvement selectivity of DA detection. Mn-doped *MoS*<sub>2</sub> (Mn-*MoS*<sub>2</sub>) has a binding energy of 0.65 eV for physisorption.[141] Physisorption is crucial in catalysis because ideally, to enable more catalytic reactions, the catalytic material must effectively adsorb the target intermediates and desorb the reaction byproducts.[142] Therefore, Mn-*MoS*<sub>2</sub> is expected to be a biosensor for DA through physical adsorption only. As shown in Fig. 10b, Mn-*MoS*<sub>2</sub> occupies an energy level on the DA under neutral conditions. The DA molecule is at present in the occupied state with the maximum energy in the +1 charge state, ensuring that holes are transported there preferentially from the *MoS*<sub>2</sub>. The DA molecules on Mn-*MoS*<sub>2</sub> are allowed to be oxidized under energization, further demonstrating its application in electrochemical DA sensors. Lu et al. found that the conversion from direct semiconductor to metal after loading Au on *MoS*<sub>2</sub> nanosheets by DFT study improved the electrochemical properties of *MoS*<sub>2</sub> nanosheets, resulting in more efficient detection of DA.[143].

For diagnostic reasons, keeping track of free radical generation at the cellular level is crucial. Gupta et al. investigated the mechanism and size-dependent sensitivity of *MoS*<sub>2</sub> to free radicals by DFT-PBE.[144] DOS analysis showed that as nanoparticle size grows, the occupied d-state peaks close to the Fermi energy level (*E*<sub>F</sub>) flatten out and move away from the *E*<sub>F</sub>, indicating that bigger particles have been lower catalytically active than smaller ones. It shows that the preferential adsorption of *H*<sub>2</sub>*O*<sub>2</sub> on the Mo edge is caused by a shift in the electron density of Mo atoms near the edge (Fig. 10c). Moreover, *MoS*<sub>2</sub> nanoparticles containing sulfur vacancies have significant catalytic activity, making them useful for ultra-low detection of a variety of compounds of biological significance.

Nanosensor-based exhaled breath analysis is a practical and quick approach for lung cancer early diagnosis. Three common exhaled volatile organic compounds (VOCs), *C*<sub>3</sub>*H*<sub>4</sub>*O*, *C*<sub>3</sub>*H*<sub>6</sub>*O*, and *C*<sub>5</sub>*H*<sub>8</sub>, have been employed as biomarkers for lung cancer detection using aluminum-doped *MoSe*<sub>2</sub> (Al-*MoSe*<sub>2</sub>).[145] The doping of Al atoms on the surface of Se vacancies of *MoSe*<sub>2</sub> improves the electrical conductivity of the material as an electron donor. Al-*MoSe*<sub>2</sub> shows admirable *C*<sub>3</sub>*H*<sub>4</sub>*O*, *C*<sub>3</sub>*H*<sub>6</sub>*O*, and *C*<sub>5</sub>*H*<sub>8</sub> sensing properties with responses of -85.7, -95.6, and -96.3%, respectively. Significantly, the recovery times for the desorption of all three VOCs by the Al-*MoSe*<sub>2</sub> were acceptable as the temperature was increased to 598 K (Fig. 10d).

The detection of acetone in human breath is suitable for non-invasive diagnosis of diseases such as diabetes and lung cancer. Yadav et al.

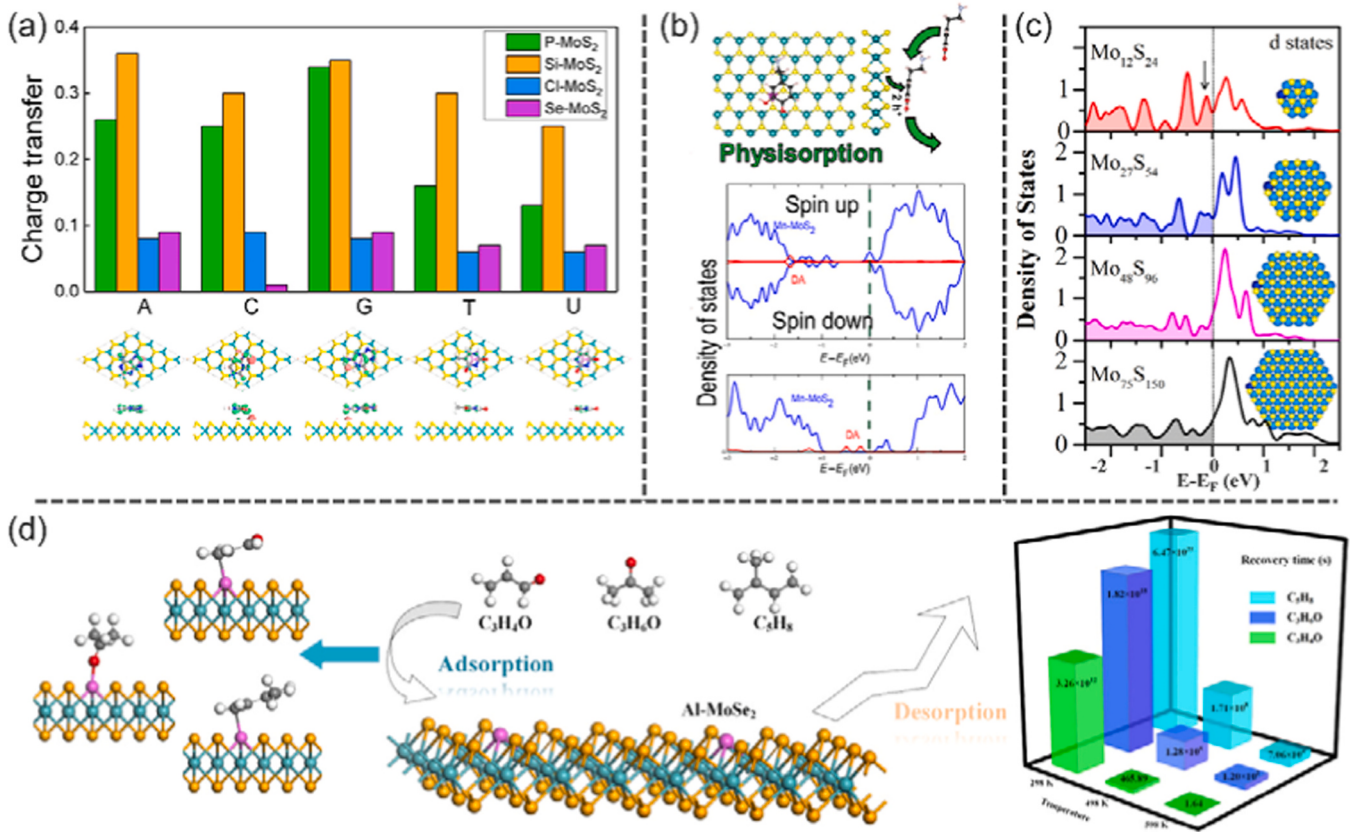


**Fig. 10.** a) Charge transfer value of X-MoS<sub>2</sub> and differential electron density of P-MoS<sub>2</sub>. a) Reproduced with permission.[140] Copyright 2019, American Chemical Society. b) DOS of DA molecules and MoS<sub>2</sub> in the natural and + 1 charge states. b) Reproduced with permission.[141] Copyright 2020, Science. c) DOS of Mo atoms at different sizes. c) Reproduced with permission.[144] Copyright 2017, IOP Publishing. d) Schematic diagram of the graphene/h-BN-based SET device. d) Reproduced with permission.[145] Copyright 2021, Elsevier.

prepared an excellent acetone-selective sensor based on WO<sub>3</sub>/WS<sub>2</sub> nanosheets.[146] The sensing results showed that the sensor responses were 132.5 and 17.0 when the acetone concentration was 1000 and 1 ppm, respectively. Combined with DFT to deeply explore the sensing mechanism, the energy gap of acetone will also change on WO<sub>3</sub>/WS<sub>2</sub> (from 2.47 to 1.31 eV), and the sensor response rate is as high as 46.98%. Similarly, the sensing performance of N-doped WS<sub>2</sub> monolayers (N-WS<sub>2</sub>) for typical lung cancer biomarkers (2,3-dimethylhexane, styrene, and toluene) was carried out by DFT-PBE calculations.[147] It was found that the conductivity change ratio which is tunable by an external operating voltage thus obtaining a direct signal from the sensor, comes to the exhaled breath of a healthy person and a lung cancer patient, i.e., at a voltage of 1.7 V, the N-WS<sub>2</sub> has a rate-of-change response difference of about 1%.

TMDCs are a layered structure with weak van der Waals forces between the layers, which easily exfoliate to an ultrathin monolayer structure and yield excellent sensing properties. For example, the detection of DNA and VOCs on their surfaces can be used for gene sequencing, rapid and sensitive non-invasive diagnosis of diseases such as liver cancer, diabetes, and lung cancer. Theoretical calculations provide atomic scale insights such as feasibility analysis of adsorption processes, adsorption-induced conductivity changes, and accurately give the response rate of the sensing molecule. This provides insights into the electronic nature of the sensing mechanism of TMDCs, thus paving the way for practical applications of TMDCs in device design and medical diagnostics.

#### Computational TMDCs as nanozyme

TMDCs have potential as nanozymes due to active edge sites and

surface electron transfer capabilities.[148] MoS<sub>2</sub> is excellent to be utilized as a POD-like nanozyme since it originates from the catalytic activity of the edge sites.[149] Defective engineering disturbs the surface of the intrinsic structure, thereby increasing the surface area of the catalytic site, thereby significantly improving the performance of the nanozyme.[150] Cao et al. constructed three typical MoS<sub>2</sub> models (pristine MoS<sub>2</sub>, S-defect MoS<sub>2</sub>, and edge MoS<sub>2</sub>) to explore the H<sub>2</sub>O<sub>2</sub> activation process (adsorption-homolysis-desorption).[151] According to Fig. 11a, the adsorption energies of H<sub>2</sub>O<sub>2</sub> at MoS<sub>2</sub> and S-defect MoS<sub>2</sub> edges are -0.14, -0.32, and -0.47 eV, respectively, indicating stable adsorption of H<sub>2</sub>O<sub>2</sub>. Activated H<sub>2</sub>O<sub>2</sub> molecules of S-defect MoS<sub>2</sub> and MoS<sub>2</sub> edge readily dissociate through the homolytic pathway to yield 2OH<sup>\*</sup>. In contrast, the hydroxyl radical desorption from MoS<sub>2</sub>, S-defect MoS<sub>2</sub>, and MoS<sub>2</sub> edge is difficult because it is a heat-absorbing reaction. The reaction energy of the total reaction (H<sub>2</sub>O<sub>2</sub> → 2OH<sup>\*</sup> → OH<sup>\*</sup> + •OH) are 1.92, -0.82, and -0.26 eV in MoS<sub>2</sub>, S-defect MoS<sub>2</sub>, and MoS<sub>2</sub> edge, respectively. This suggests that s-defective MoS<sub>2</sub> and MoS<sub>2</sub> edges contribute to the improvement of the H<sub>2</sub>O<sub>2</sub> degradation process, especially in s-defective MoS<sub>2</sub>. Subsequently, MoS<sub>2</sub> with S and Mo vacancies in the MoS<sub>2</sub> model (perfect MoS<sub>2</sub>, S vacancy MoS<sub>2</sub> (V<sub>S</sub>), and MoS<sub>2</sub> with Mo and S vacancy (V<sub>Mo</sub> + V<sub>S</sub>)) to probe the POD degradation mechanism. The usual POD degradation pathways are shown in the following Eq. (8) ~ (11), which correspond to pathways I-IV in Fig. 11b, respectively. It can be seen that although the V<sub>Mo</sub> + V<sub>S</sub> lattice produces •OH both in pathway I and pathway II, the amount produced by pathway I is greater. Moreover, the •OH desorbed by V<sub>Mo</sub> + V<sub>S</sub> under Pathway I and Pathway II conditions is hardly free to proceed. And the amount of O<sub>2</sub> degraded by H<sub>2</sub>O<sub>2</sub> is limited as seen by Pathway III and IV. The reaction between the MoS<sub>2</sub> model and O<sub>2</sub> was further explored (Eq.12), and all models produced •OH spontaneously, but the amount of V<sub>Mo</sub> + V<sub>S</sub> was greater

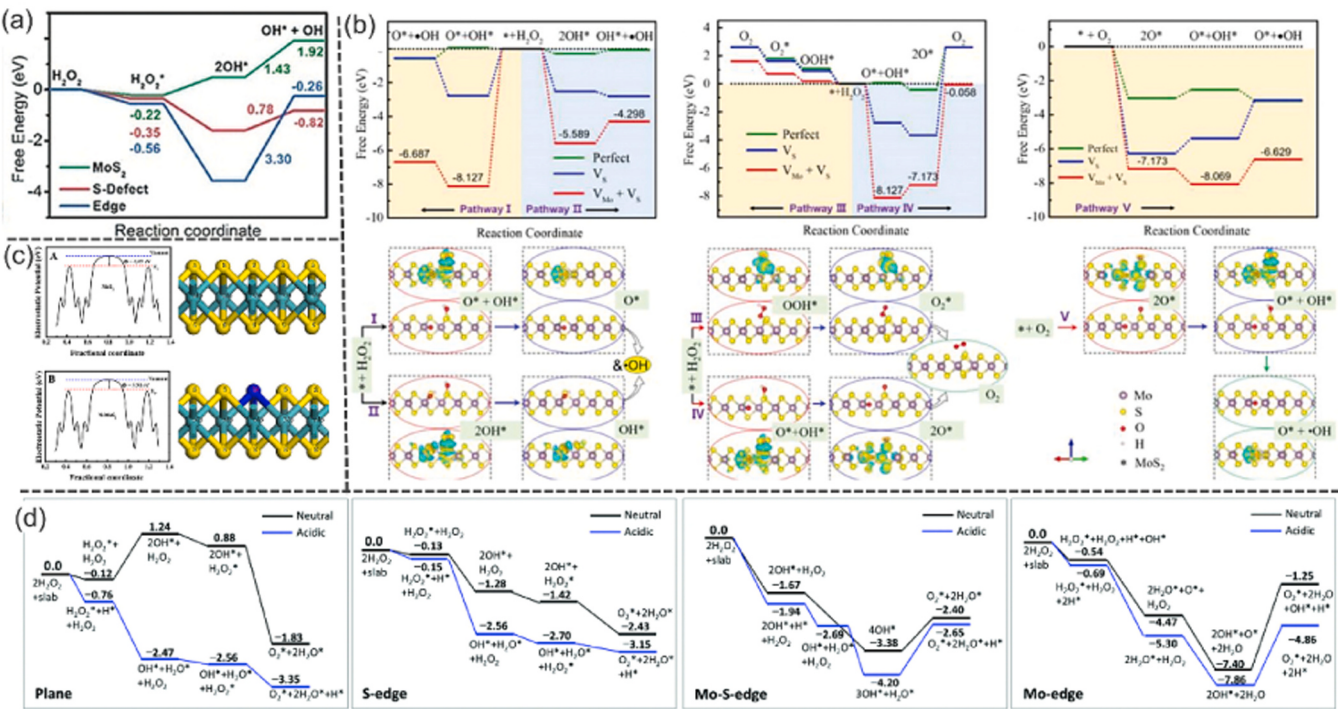
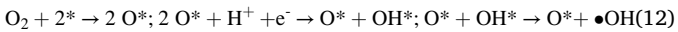
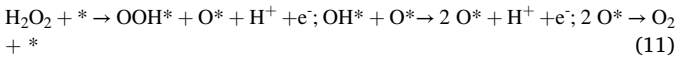
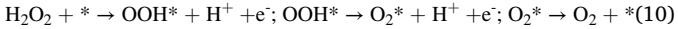
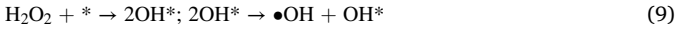


**Fig. 11.** a) Energy profiles of pristine, S-defect, and edge MoS<sub>2</sub> in catalytic process. a) Reproduced with permission.[151] Copyright 2019, Wiley. b) The free energy diagrams of MoS<sub>2</sub> models for the production of •OH and the corresponding charge density difference of the V<sub>Mo</sub> + V<sub>s</sub> model. b) Reproduced with permission.[148] Copyright 2020, Wiley. c) Work functions and models of MoS<sub>2</sub> and N-doped MoS<sub>2</sub>. c) Reproduced with permission.[152] Copyright 2020, American Chemical Society. d) Free energy diagram for disproportionation of H<sub>2</sub>O<sub>2</sub> on MoS<sub>2</sub> with different end faces. d) Reproduced with permission.[156] Copyright 2021, Royal Society of Chemistry.

(Fig. 11b).



In addition to the above defective MoS<sub>2</sub> nanzymes, heteroatoms have also been introduced into MoS<sub>2</sub>. Feng et al. modified the catalytic activity of MoS<sub>2</sub> by changing its electronic structure through N-doping. [152] MoS<sub>2</sub> and N-doped MoS<sub>2</sub> exhibit work functions of 4.47 eV and 5.20 eV, respectively (Fig. 11c). The Fermi level closer to the valence band can be attained for N-doped MoS<sub>2</sub>, which can promote charge transfer, and thus greatly improve the catalytic activity of N-doped MoS<sub>2</sub>. Furthermore, the POD-like activity of MoS<sub>2</sub> doped with various transition metal atoms was also investigated. [153] The catalytic activity of Fe, Cu, and Co-doped MoS<sub>2</sub> towards H<sub>2</sub>O<sub>2</sub> is dramatically increased as compared to pure MoS<sub>2</sub>, among which Co-doped MoS<sub>2</sub> material has the highest activity. The results show that the metal abundance in MoS<sub>2</sub> increases with the doping of transition metals. The desorption of reactants is more favorable the further away the d-band center goes from the Fermi level, and the d-band centers of MoS<sub>2</sub>, Ni, and Co-doped MoS<sub>2</sub> are -0.284, -0.697, and -0.728 eV, respectively. Thus, transition metal doping makes MoS<sub>2</sub> have higher catalytic activity.

Multiple antioxidant nanzymes work together to keep intracellular redox equilibrium stable during ordinary physiological activities by removing reactive oxygen species (ROS) in a well-controlled cascade reaction. [154] However, as the disease progresses, these enzymes are often not adequately replenished by excessive ROS production. [155] Therefore, catalytic ROS scavenging therapies using multienzyme

complexes are required. [94] Multiple antioxidant MoS<sub>2</sub> form a self-cascading platform for scavenging excess intracellular ROS to inhibit ROS production. Zhang et al. revealed the atomic-level mechanism of the interaction between MoS<sub>2</sub> nanoparticles and H<sub>2</sub>O<sub>2</sub> under both neutral and acidic conditions on various exposed surfaces by means of DFT calculations. [156] The protonated substrate is thermodynamically favorable for O-O bond cracking and O<sub>2</sub><sup>\*</sup> creation, while the protonation of the S-side further promotes the generation of O<sub>2</sub><sup>\*</sup> (Fig. 11d). The Mo-S edge and Mo-edge of the pre-adsorbed protons remain inactive in the generation of O<sub>2</sub><sup>\*</sup>. These calculations suggest that the acidic conditions make the MoS<sub>2</sub> substrate thermodynamically favorable for H<sub>2</sub>O<sub>2</sub> disproportionation to O<sub>2</sub>, and improved the catalytic activity of MoS<sub>2</sub>. The S vacancies of TMDs readily capture photo-generated electrons and achieve rapid electron-hole pair separation, generating free radicals to destruct bacterial cell membranes. [157] The S vacancy-rich WS<sub>2-x</sub> and the 2D layered structure Bi<sub>2</sub>WO<sub>6</sub> form a heterojunction (Bi<sub>2</sub>WO<sub>6</sub>/WS<sub>2-x</sub>) as a broad-spectrum bactericide that effectively kill Gram-positive and Gram-negative bacteria in vivo and in vitro under simulated sunlight. ESR spectra showed a significant increase in the •OH and <sup>1</sup>O<sub>2</sub> signals of Bi<sub>2</sub>WO<sub>6</sub>/WS<sub>2-x</sub>. Combined with DFT, it was further confirmed that the binding energy of the Bi<sub>2</sub>WO<sub>6</sub>/WS<sub>2-x</sub> surface to H<sub>2</sub>O becomes lower due to the presence of S vacancies, thus promoting the generation of •OH.

Wang et al. systematically screened out two-dimensional nano-materials with sod-like activity in the Computational 2D Materials Database (C2DB, established by Thygesen et al., which stores the geometric structures and electronic properties of about 4000 different 2D materials obtained through DFT calculations [158]). [159] Firstly, the screening element less than or equal to 2 (N<sub>element</sub> ≤ 2), with excellent thermodynamic stability (ΔH<sub>hull</sub> < 0.2 eV/atom) and kinetic stability (ΔE<sub>min</sub> > 10<sup>-5</sup> eV/Å<sup>2</sup>), and a band gap not equal to zero calculated using the Heyd-Scuseria-Ernzerhof (HSE) functional (E<sub>g,HSE</sub> > 0). In addition, the screened material needs to have only one kind of iFMO (CBM or

VBM) with energies in the range ( $\varphi_1, \varphi_2$ ), and the Gibbs free energy was also used as a screening criterion, ie.  $E_{\text{ads},\text{HO}} > -2.7$  eV and  $E_{\text{ads},\text{H}} > -3.4$  eV. Screened out 121 materials with sod-like nanzyme activity according to the quasi-aforementioned criteria, including T-phase t TMDCs (PtS<sub>2</sub>, ZrS<sub>2</sub>, ZrSe<sub>2</sub>, SnS<sub>2</sub>, HfS<sub>2</sub>) and H-phase TMDCs (MoTe<sub>2</sub>, WSe<sub>2</sub>, WTe<sub>2</sub>, VS<sub>2</sub>). Then Wang carried out a computational study on the sod-like activity of these nine single-layer TMDC structures, and the results were in good agreement with the predictions.

DFT calculations give a rational explanation for the reaction path design and potential energy surface of the catalytic reactions of TMDCs-based nanozymes. The close connection between accurate computational methods and advanced experimental approaches has led to the fact that the DFT mechanism and kinetics of nanozymes have been extensively studied. Meanwhile, the development of machine learning has likewise brought light to the design and development of model predictions for TMDCs nanozymes with excellent performance.

#### Computational TMDCs for drug delivery

Thin-layer TMDCs have several excellent characteristics that make them appropriate for drug delivery applications.<sup>[160]</sup> Mohammed et al. investigated the interaction of bilayer MSe<sub>2</sub> and MS<sub>2</sub> (M=Mo and W) on  $\beta$ -lap anticancer drugs using DFT method.<sup>[161]</sup> The formation energy results show that for MoS<sub>2</sub>/ $\beta$ -lap, MoSe<sub>2</sub>/ $\beta$ -lap, WS<sub>2</sub>/ $\beta$ -lap and WSe<sub>2</sub>/ $\beta$ -lap, the corresponding values are equal to  $-3.105$ ,  $-2.449$ ,  $-2.835$ , and  $-2.284$  eV, respectively, the negative values indicate that all composite systems are thermodynamically stable. The MoS<sub>2</sub>/ $\beta$ -lap system has a lower formation energy than the other systems, which suggests that  $\beta$ -lap interacts with MoS<sub>2</sub> more strongly. The two-dimensional complexes exhibit insulating behavior with strong kinetic, thermal and mechanical stability. Liang et al. investigated the geometrical structure, electronic characteristics, and optical properties of some novel anti-tuberculosis drugs (drugs isoniazid (INH), pyrazinamide (PZA), and PZA/INH) on MoS<sub>2</sub>, and the effect of temperature and pH on the adsorption capacity for effective drug delivery.<sup>[162]</sup> When bound to MoS<sub>2</sub>, all antitubercular drugs exhibited physisorption properties, but the mixed INH/PZA showed the highest formation energy at the interface due to charge transfer. The system exhibits

insulating behavior after the adsorption of drug molecules on molybdenum disulfide with strong kinetic, thermal, and mechanical stability. INH and PZA readily desorb from the MoS<sub>2</sub> surface under high temperatures and acidic conditions. Therefore, MoS<sub>2</sub> has potential applications for precisely targeted drug delivery.

#### Advances in the calculation of Xenes for bioapplications

##### Structure and electronic properties of Xenes

Similarly, 2D Xenes are predicted to have curved, planar, and folded geometries (Fig. 12).<sup>[163]</sup> Their hybridization states are  $sp^2$ ,  $sp^3$ , and between  $sp^2$  and  $sp^3$ , leading to various 2D isomeric structures, and anisotropy. Unlike other 2D materials, Xenes have unique electronic properties, and to a large extent the non-use of such properties depends on the X element. By varying the X-atom species in Xenes, metallic, semiconductor, or insulator properties can be achieved, e.g., borylene is a metal, silicene is a semimetal and styrene is an insulator<sup>[164,165]</sup> Key properties of Xenes for biomedical applications include its environmental stability and biosystem degradability.<sup>[166]</sup> Even though some Xenes are unstable in water or the atmosphere, functionalization of its surface enhances stability. Furthermore, their low stability may offer special benefits in medicinal applications by facilitating their metabolism and breakdown in living organisms.

##### Theoretical investigation of Xenes in bioapplications

##### Computational Xenes as biosensor

Xenes are 2D single-element nanomaterials. They include arsenene, antimонene, germanene, phosphorene, borophene and silicene. They have unique potential in various biomedical applications. Amino acid moieties such as Glycine (Gly), glutamic (Glu), histidine (HIE), and phenylalanine (Phe) adsorbed onto puckered antimонene for biomedical sensing were studied.<sup>[167]</sup> All amino acids exhibited physical adsorption on antimонene, with Phe having the most favorable adsorption energy of  $-0.43$  eV. The direct band gap of antimонene was only  $0.24$  eV, but it was reduced to  $0.233$  eV,  $0.23$  eV,  $0.222$  eV, and  $0.041$  eV by adsorption with amino acids Glu, Gly, Phe, and HIE,

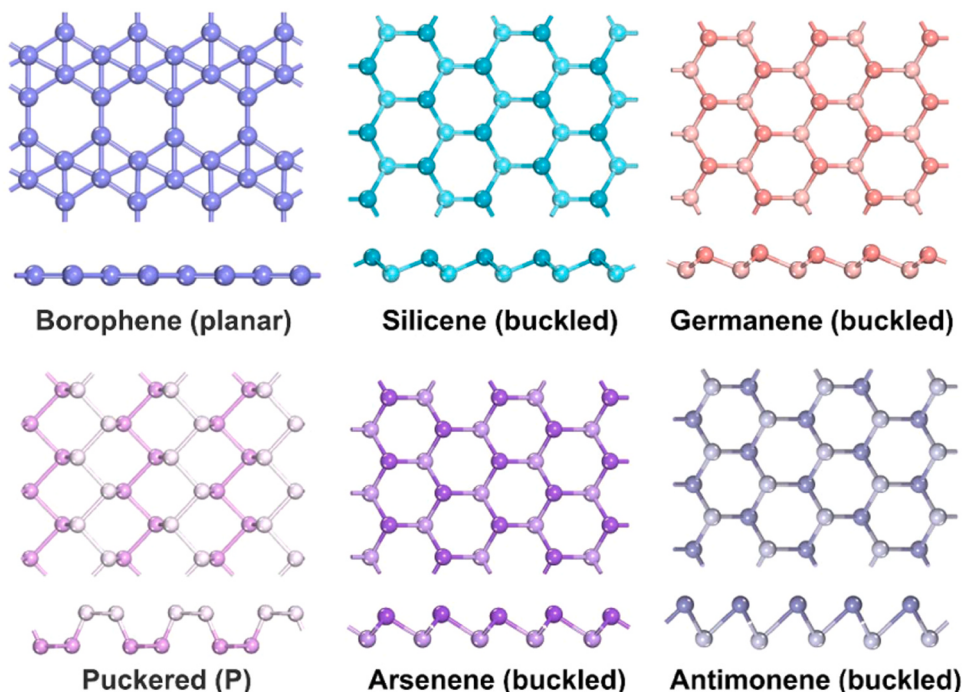


Fig. 12. The geometric structure of Xenes is common in biological applications.

respectively. According to their optical makeup, all systems exhibit maximum absorption close to the visible range where there is the least energy loss. Consequently, antimonene is also suitable for devices such as biosensors and biointegrated electronics-based devices.

Surface Plasmon Resonance (SPR) technique has many advantages such as label-free detection, high repetition rate and affordability to study molecular interactions has been applied in biosensors. Xu et al. employed antimonene to prepare SPR sensors and performed quantitative analysis of miRNA molecules on their surfaces.<sup>[168]</sup> As shown by the test results of SPR spectra, for the detection of target miRNA-21 at very low concentrations of  $10^{-17}$  M, the SPR angle undergoes a significant left shift. In addition, the use of base mismatched miRNAs also leads to a shift in the SPR angle thus enabling the detection of nucleobase mutations. DFT-based calculations found that antimonene interacts much more strongly with single-stranded DNA than graphene, which was previously used for DNA molecule sensing, thanks to more off-domain 5 s/5p antimonene orbitals. Roknabadi et al. used the DFT-D2 method within the PBE framework to consider van der Waals interactions of germanene on amino acids and demonstrated that germanene exhibited high sensitivity to amino acids.<sup>[169]</sup> Meanwhile, DFT and NEGF-based studies have shown that both silicene and germanene are good candidates for DNA/RNA rapid sequencing device applications.<sup>[170]</sup> Similarly, borophene,<sup>[171]</sup> tellurene,<sup>[172]</sup> and phosphorene<sup>[173]</sup> are potential biosensors for DNA/RNA and amino acid molecule detection.

Chandiramouli et al. performed a study of black phosphorus flakes (B-Ph) as sensors for biomarkers of liver cancer (e.g. 1-Octen-3-ol, hexanal, decane).<sup>[174]</sup> Liver cancer biomarker volatiles are physically adsorbed at B-Ph. Moreover, the BP band gap was altered from its initial 0.889 eV to a range of 0.798 ~ 0.906 eV as a result of the adsorption of biomarkers (Fig. 13a). Charge transfer and electron density also cause deviations with the adsorption of liver cancer volatiles. Furthermore, they investigated that Beta arsenene nanosheet (As-NS) were used as substrates for the adsorption of tuberculosis (TB) biomarkers, namely hexylcyclohexane, 4-methyldodecane, oxetane, 3-(1-methylethyl), and tridecane.<sup>[175]</sup> The As-NS material has a band gap of 0.635 eV and has semiconductor properties with physisorption energy of biomarkers between  $-0.198 \sim -0.516$  eV. It is noteworthy that the As-NS electronic

properties change in energy band structure with the TB biomarker molecule (Fig. 13b).

Xenes have diverse surface chemical modifications enabling the adsorption of biomarkers, which promises applications in biosensors. Theoretical calculations of electron transfer and charge interactions between Xene materials and sensing recognition molecules are crucial for understanding the sensing mechanism. The computational outcomes of Xene applications on biosensors such as adsorption type, sensitivity, band gap and other properties are very useful for the experimenter to design a Xenes based sensor.

#### Computational Xenes for drug delivery

Hashemzadeh et al. studied the delivery efficiency of the anticancer drug melanophene; 6-thioguanine (TG) using MD simulations and DFT methods.<sup>[176]</sup> MD simulations indicated that complexes of phosphorene (Ph) with TG would display spontaneous diffusion in lipid bilayers. This property can be exploited to deliver anticancer drugs to cellular targets. Overall, the results suggest that TG is physisorbed on the surface of Ph, and the phosphorene-drug complex can be used as a DDS. Recently, they also explored the dual delivery of the anticancer drugs paclitaxel (PTX) and DOX by h-BN and BP nanosheets using MD simulation, as well as investigated the mechanisms behind their adsorption on the carrier.<sup>[177]</sup> Tariq et al. evaluated the effectiveness of Ph as a drug delivery system, the geometric, electronic, and excited state features of chlorambucil, phosphorene (Ph), and Ph-chlorambucil complexes.<sup>[178]</sup> Frontier molecular orbital analysis shows that during HOMO to LUMO excitation, the charge is transferred from chlorambucil to Ph. The excited state calculations showed that these weak intermolecular forces facilitate drug release on the target. In conclusion, phosphorene has prosperous therapeutic potential as a drug carrier for chlorambucil in targeted cancer therapy. Phosphorene can also be used as a suitable nanocarrier for the delivery of thioguanine drug molecules, which are physically adsorbed and have high dipole moments (1.74 D) phosphorene-thioguanine complex showed higher biodegradability.<sup>[179]</sup> Phosphorene is a candidate for therapeutic potential as a novel carrier for the delivery of cardiovascular drugs (carvedilol, felodipine). DFT theoretical research suggests that phosphorene can be used as an

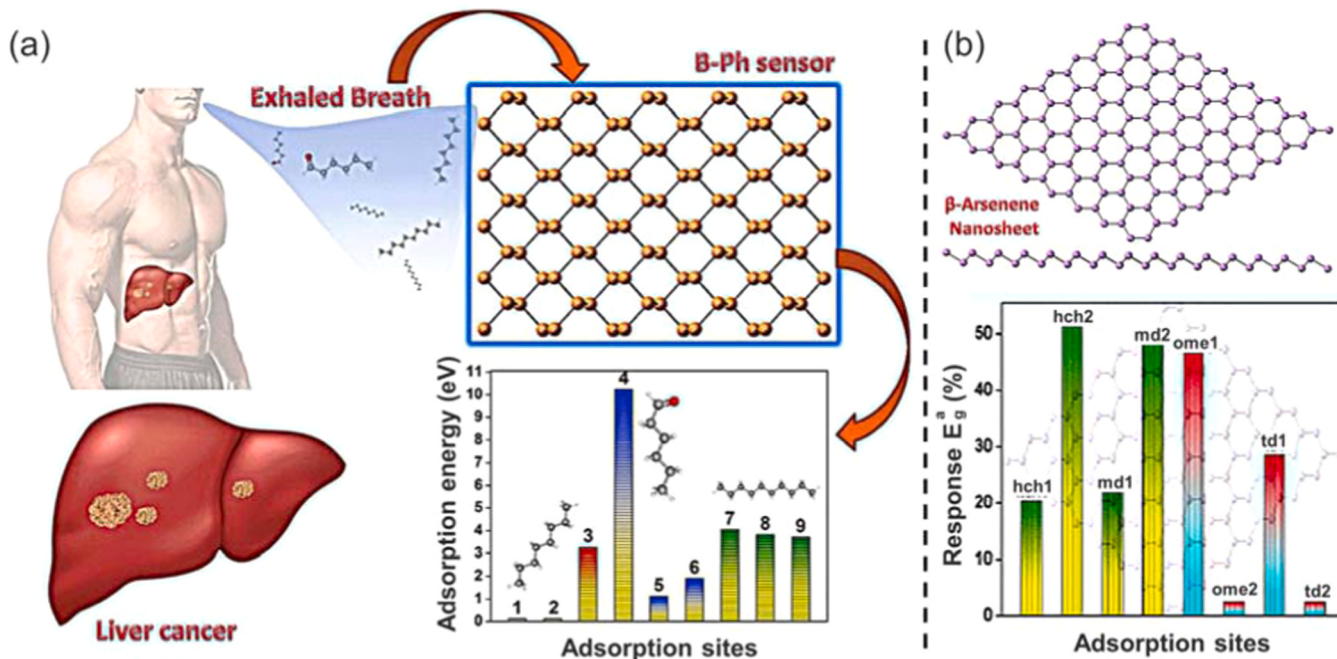


**Fig. 13.** Illustrations of a) B-Ph as a biosensor for liver cancer and b) As-NS as a biosensor for tuberculosis. a) Reproduced with permission.<sup>[174]</sup> b) Reproduced with permission.<sup>[175]</sup> Copyright 2021, Elsevier.

effective vehicle for delivering therapeutic drugs to treat cardiovascular disease.[180,181].

Modification of silicene by various functional groups is a common means to improve its drug loading efficiency. The properties of DOX-loaded polyethyleneimine (PEI) functionalized phosphorene (PEI-Ph) as a drug delivery system were investigated.[182] The findings demonstrated that the drug was adsorbed on the surface of PEI-Ph through  $\pi$ - $\pi$  interactions. MD simulations showed that, unlike isolated DOX, the drug complexed with PEI-Ph could easily penetrate the cell membrane. Razavi et al. modified silicene nanosheets (SNS), such as folic acid functionalized SNS and PEI functionalized SNS, to study the surface loading/release mechanism of anticancer drugs (PTX, Anastrozole (ANA), and Mefaram (MEL)).[183,184].

Similar to the graphene mentioned above, Xenes also use doping to improve the drug-loading performance of the carrier. DFT simulations to examine the potential for drug delivery of Ifosfamide (IFO) with initial PH and alkaline earth metals (M = Be, Mg, and Ca) doped with Ph (M-Ph).[185] The IFO@M-PH system has higher adsorption energy than the undoped system. After doping, the polarity of drug carrier system is increased, which is conducive to effective drug flow in vivo. Among the doped complexes, Ca doping system shows excellent performance. Similarly, Mahboobi et al. examined the adsorption of mercaptopurine and fluorouracil on phosphene and Ca-, Na- and Fe doped phosphorene at the B3LYP/6-31 G (d) level of the DFT method.[186] The calculation showed that Ca-doped phosphorene also showed the best performance in drug delivery performance compared with Na and Fe doping.

#### Computational Xenes for photodynamic therapy (PDT)

Photodynamic therapy (PDT) is an innovative alternative cancer therapy that utilizes the interaction of light and matter.[187] This treatment is used for cancer treatments such as skin, esophageal, lung, and bladder cancers and for non-malignant diseases such as fungal strains, bacterial infections, and viral infections.[188] In theory, PDT includes the interplay of three key components, namely the photosensitizer (PS), light (of the appropriate wavelength) and oxygen ( $O_2$ ). In particular, PS produces cytotoxicity through the production of reactive oxygen species (ROS), which causes fast cell death through apoptosis or

necrosis. With its unique monolayer structure and the excellent biosafety of its single element, Xenes holds exciting promise for biomedical applications. However, the non-semiconductor nature of Xenes limits their potential biological applications such as biosensors, bioimaging, and phototherapy.

Recently, Fig. 14a showed the optimized structure of H-germanene with hydrogen capped germanene for energy band tuning of germanene. [189] The results of DOS calculations based on Heyd-Scuseria-Ernzerhof (HSE06) show that the bandgap of the intercalated delaminated H-germanene is 1.55 eV, suggesting that the modification of H is responsible for the opening of the bandgap in the h-germanene from the zero-bandgap conductor of pristine germanium (Fig. 14b). The energy level of the H-Ge- $O_2$  T<sub>1</sub> excited state complexes have an energy level of 1.85 eV (Fig. 14c). Subsequently, electron transfer produces the intermediate state of H-Ge- $O_2$ <sup>+</sup>. With the goal to attain a thermodynamically advantageous energy state,  $^1O_2$  is finally liberated from the H-germanene- $O_2$ <sup>+</sup> state. Similarly, H-functionalized silicene nanosheets thus lead to the transformation of the original zero-bandgap structure into a direct bandgap semiconductor structure (bandgap 2.4 eV) and can achieve efficient PDT by generating ROS based on its semiconductor properties (Fig. 14b). [190].

#### Conclusions and outlook

Recently, theoretical computing has played a key part in the investigation and development of 2D materials for biological applications. It not only provides insight into reaction mechanisms and kinetics but also allows comprehensive prediction of 2D materials' geometry, electronic structure changes and interactions between the guest and the carrier, as well as kinetic stability over time. Computational studies bridge the gap between macroscopic experimental trends and microstructures to some extent. When it comes to different biological applications, the main calculations are both cross-cutting and different (Fig. 15). By performing calculations of multiple properties, we can gain a more comprehensive perspective to understand the role of 2D materials in corresponding biological applications, providing deeper and more comprehensive insights.

Despite the current critical issues and technical challenges, these

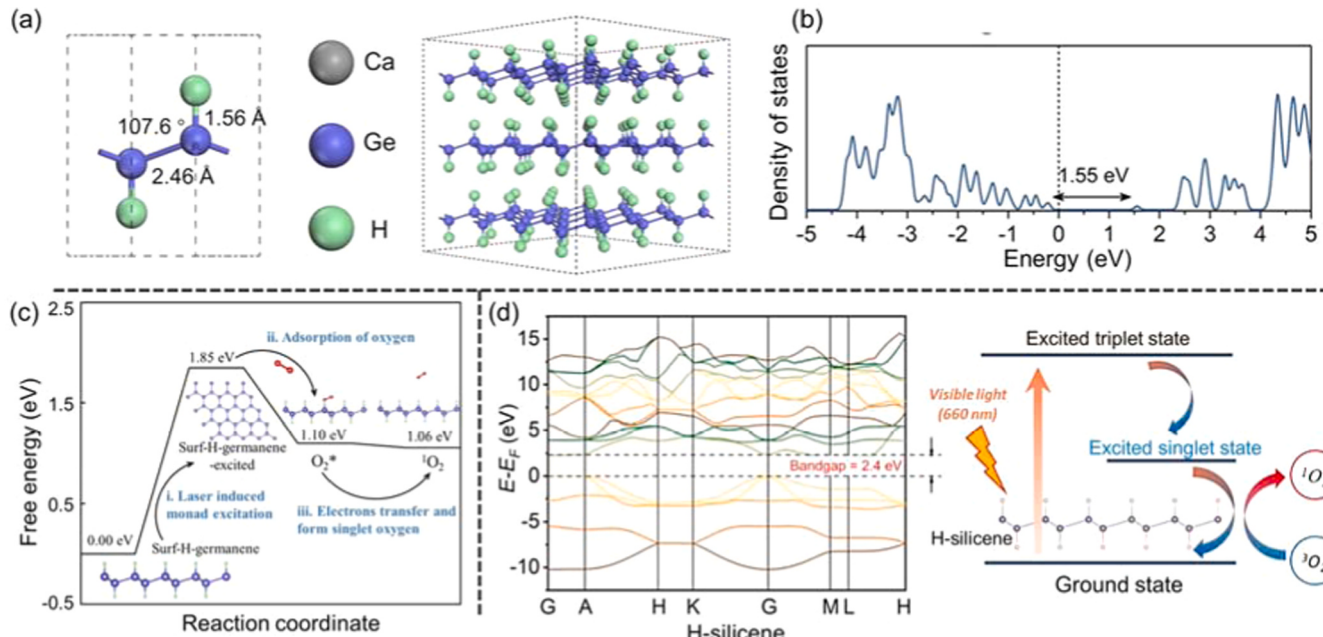
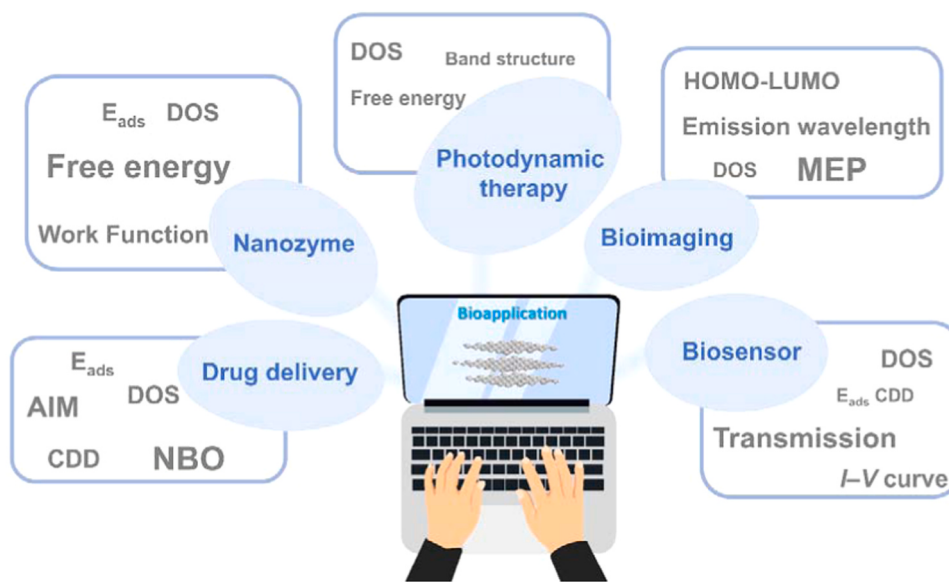


Fig. 14. a) Optimized structure of H-germanene, b) DOS, and c) schematic diagram of H-germanene photocatalytic single linear state oxygen generation mechanism. a-c) Reproduced with permission.[189] Copyright 2023, Wiley. d) Band structure of H-silicene and the mechanism of ROS generation d) Reproduced with permission. [190] Copyright 2021, Elsevier.



**Fig. 15.** A summary of computational content for various biomedical applications of computational 2D materials.

computational simulation methods are flourishing for the future of 2D materials in biological applications. Currently, computational simulations are mainly used to assist in verifying unanswered questions and explaining potential mechanisms during experiments, requiring theoretical findings to indicate the direction of the experiment, solve difficult problems, and reduce research costs and human investment. Furthermore, the development and evaluation of computational methods capable of handling complex biological systems is an important future task. Thus, 2D materials still face some pressing problems in biocomputing:

- (1) For theoretical work, a careful selection of exchange-correlated functional is necessary, utilizing the various complex corrections available, such as hybrid functional, Hubbard  $U$  parameter, as well as dispersion corrections. Theoretical work enables to identification of the most suitable 2D materials for biological applications and provides relief for experimentalists who have difficulty exploring all possibilities. Many biological applications of 2D materials require significant effort and funding for pre-experimental exploration, so theoretical work can prioritize and point the way to exploring the feasibility for pre-experimental biological exploration.
- (2) The living organism is a complex system involving many biochemical processes and interactions between molecules. This means that a great deal of computational resources and time are required to perform accurate simulations and calculations. Researchers are working on developing enhanced sampling methods to accurately characterize the computational content with some success. However, the currently available force fields still have some limitations, especially for complex biological systems and environments. Therefore, improving the accuracy and validity of force fields remains a challenge.
- (3) 2D biomaterials present potential for a wide range of biomedical applications, but their biological toxicity requires attention. These materials are typically administered intravenously, orally, or implanted into biosensors and bioimaging devices to target critical organs. Consequently, a comprehensive biosafety assessment must be performed before 2D materials undergo successful translation into clinical applications. To this end, the establishment of databases containing biological toxicity, preparation methods, electronic properties, biological properties, etc. is necessary and urgent. Moreover, these databases are the basis for

high-throughput computation or screening, which helps researchers to quickly and accurately screen safe biologic 2D materials with specific functions.

- (4) Computational science cannot be separated from practical experimental applications, and macroscopic experiments need to be supported by theoretical results. Interdisciplinary collaboration between biology and computational science has great potential for solving complex biological problems; yet, the lack of in-depth learning at the intersection of multiple disciplines may lead to a deficiency of deep and thorough insights. Biologists without a computational background may have difficulty understanding complex computational results and relating them to experimental results, which is undoubtedly a major obstacle to a complete understanding and precise interpretation of the research problem. Consequently, interdisciplinary research needs to be encouraged so that researchers with specialized backgrounds in biology and computational science get practical experience in solving problems encountered in their research in a collaborative process.

In summary, the most effective way to develop future 2D materials for biological applications is a combination of theoretical calculations and experiments. In order to better advance the research, we are keen to create a database with good structural, electronic properties, and biological toxicity. The development of accurate force fields and biological models capable of handling larger biological systems is also a future task. Due to the diversity of 2D materials, designing appropriate biological applications based on preliminary laboratory work is a future challenge, and research in areas such as machine learning for developing empirical activity descriptors that effectively predict the feasibility of 2D materials for a wide range of biological applications deserves special attention in the future. [Table 1](#).

#### CRediT authorship contribution statement

**Yinyin Qian:** Investigation, Visualization, Writing – original draft.  
**Huaming Yang:** Conceptualization, Supervision, Writing – review & editing, Project administration, Funding acquisition. All authors discussed the results, revised or commented on the manuscript.

**Table 1**

A summary of representative computational 2D carbon-based nanozymes.

Nanozymes	Active center	Substrate	Mimic function	Bioapplications	Functional	Ref
GO	C=O	GO	POD	/	DFT-	[98]
N,B codoped rGO	B,N	rGO	POD	/	DFT-PBE	[100]
B-doped Fe-N-C nanozyme	FeN <sub>4</sub> B <sub>2</sub>	/	POD	Enzyme activity and small molecule detection	GGA-PBE	
B doped graphdiyne	B	GDY	POD	antibacterial	GGA-PBE	[104]
S doped graphdiyne	S	GDY		Antibacterial	GGA-PBE	[191]
N,B codoped graphdiyne	B, N	GDY	POD	cancer therapy	GGA-PBE	[105]
Pd, Fe decorated graphdiyne	Pd, Fe	GDY	POD	antibacterial	GGA-PBE	[192]

**Declaration of Competing Interest**

The authors declare that they have no known competing financial interests or personal relationships that could have appeared to influence the work reported in this paper.

**Data availability**

No data was used for the research described in the article.

**Acknowledgments**

This work was supported by the National Key Research and Development Program of China (2022YFC2904804), CUG Scholar Scientific Research Funds at China University of Geosciences (Wuhan) (2019152), the Fundamental Research Funds for the Central Universities at China University of Geosciences (Wuhan) and the National Science Fund for Distinguished Young Scholars (51225403).

**References**

- [1] X. Wang, X. Han, C. Li, Z. Chen, H. Huang, J. Chen, C. Wu, T. Fan, T. Li, W. Huang, O.A. Al-Hartomy, A. Al-Ghamdi, S. Wageh, F. Zheng, A.G. Al-Sehemi, G. Wang, Z. Xie, H. Zhang, *Adv. Drug Deliv. Rev.* 178 (2021), 113970.
- [2] A.V. Pradeep, S.V. Satya Prasad, L.V. Suryam, P. Prasanna Kumari, *Mater. Today Proc.* 19 (2019) 380–383.
- [3] Y. Wang, M. Qiu, M. Won, E. Jung, T. Fan, N. Xie, S.-G. Chi, H. Zhang, J.S. Kim, *Coord. Chem. Rev.* 400 (2019), 213041.
- [4] R. Kurapati, K. Kostarelos, M. Prato, A. Bianco, *Adv. Mater.* 28 (2016) 6052–6074.
- [5] C. Du, T. Du, Z. Chang, C. Yin, Y. Cheng, *Adv. Drug Deliv. Rev.* 186 (2022), 114314.
- [6] J. Ouyang, S. Rao, R. Liu, L. Wang, W. Chen, W. Tao, N. Kong, *Adv. Drug Deliv. Rev.* 185 (2022), 114268.
- [7] C. Martín, K. Kostarelos, M. Prato, A. Bianco, *Chem. Commun.* 55 (2019) 5540–5546.
- [8] L. Ma, X. Song, Y. Yu, Y. Chen, *Adv. Mater.* 33 (2021), 2008226.
- [9] F. Meng, M. Peng, Y. Chen, X. Cai, F. Huang, L. Yang, X. Liu, T. Li, X. Wen, N. Wang, D. Xiao, H. Jiang, L. Xia, H. Liu, D. Ma, *Appl. Catal. B* 301 (2022), 120826.
- [10] X. Shen, Z. Wang, X.J. Gao, X. Gao, *Adv. Mater.* (2023), 2211151.
- [11] Z. Li, Y. Zhang, C. Chan, C. Zhi, X. Cheng, J. Fan, *ACS Nano* 12 (2018) 2764–2772.
- [12] X. Dai, Y. Chen, *Adv. Mater.* 35 (2023), 2204798.
- [13] J.P. Perdew, K. Burke, M. Ernzerhof, *Phys. Rev. Lett.* 77 (1996) 3865–3868.
- [14] H. Sun, *J. Phys. Chem. B* 102 (1998) 7338–7364.
- [15] J. Huang, A.D. MacKerell Jr, *J. Comput. Chem.*, 34 (2013) 2135–2145.
- [16] J.R. Maple, M.-J. Hwang, T.P. Stockfisch, U. Dinur, M. Waldman, C.S. Ewig, A. T. Hagler, *J. Comput. Chem.* 15 (1994) 162–182.
- [17] R.T. Cygan, J.-J. Liang, A.G. Kalinichev, *J. Phys. Chem. B* 108 (2004) 1255–1266.
- [18] Y.-y Qian, B. Zheng, Y. Xie, J. He, J.-m Chen, L. Yang, X. Lu, H.-t Yu, *Langmuir* 37 (2021) 11027–11040.
- [19] R. Esfandiarpour, F. Badalkhani-Khamseh, N.L. Hadipour, *Colloids Surf. B* 215 (2022), 112513.
- [20] R.S. Mulliken, *J. Chem. Phys.* 23 (1955) 1833–1840.
- [21] F.L. Hirshfeld, *Theor. Chim. Acta* 44 (1977) 129–138.
- [22] G. Henkelman, A. Arnaldsson, H. Jónsson, *Comput. Mater. Sci.* 36 (2006) 354–360.
- [23] S. Srebrenik, H. Weinstein, R. Pauncz, *Chem. Phys. Lett.* 20 (1973) 419–423.
- [24] R.F. Stewart, *Chem. Phys. Lett.* 65 (1979) 335–342.
- [25] P. Politzer, J.S. Murray, *Theor. Chem. Acc.* 108 (2002) 134–142.
- [26] E. Scrocco, J. Tomasi, The electrostatic molecular potential as a tool for the interpretation of molecular properties. *New Concepts II*, Springer., 2005, pp. 95–170.
- [27] F. Biegler-König, J. Schönbohm, *J. Comput. Chem.* 23 (2002) 1489–1494.
- [28] V.V.T. Padil, K.P. Akshay Kumar, S. Murugesan, R. Torres-Mendieta, S. Waclawek, J.Y. Cheong, M. Černík, R.S. Varma, *Green Chem.* 24 (2022) 3081–3114.
- [29] A. Eckert, M. Abbasi, T. Mang, K. Saalwächter, A. Walther, *Macromolecules* 53 (2020) 1716–1725.
- [30] I. Ilić, A. Milutinović-Nikolić, Z. Mojović, Z. Vučović, P. Vučić, I. Gržetić, P. Banković, N. Jović-Jovičić, *Appl. Clay Sci.* 193 (2020), 105668.
- [31] H. Yi, X. Zhang, Y. Zhao, L. Liu, S. Song, *Surf. Interface Anal.* 48 (2016) 976–980.
- [32] Z. Xian, Y. Hao, Y. Zhao, S. Song, *Colloids Surf. A* 533 (2017) 55–60.
- [33] F. Bergaya, G. Lagaly, *Handbook of clay science*, Newnes. 2013.
- [34] E. Gianni, K. Avgoustakis, D. Papoulis, *Eur. J. Pharm. Biopharm.* 154 (2020) 359–376.
- [35] T.M. Herrington, A.Q. Clarke, J.C. Watts, *Colloids Surf. B* 68 (1992) 161–169.
- [36] M.I. Carretero, C.S.F. Gomes, F. Tateo, Chapter 5.5 - Clays, drugs, and human health, in: F. Bergaya, G. Lagaly (Eds.), *Dev. Clay Sci.*, Elsevier, 2013, pp. 711–764.
- [37] C. Bretti, S. Cataldo, A. Gianguzza, G. Lando, G. Lazzara, A. Pettignano, S. Sammartano, *J. Phys. Chem. C* 120 (2016) 7849–7859.
- [38] P. Pasbakhsh, G.J. Churchman, J.L. Keeling, *Appl. Clay Sci.* 74 (2013) 47–57.
- [39] Y.M. Lvov, D.G. Shchukin, H. Möhwald, R.R. Price, *ACS Nano* 2 (2008) 814–820.
- [40] G.I. Fakhrullina, F.S. Akhatova, Y.M. Lvov, R.F. Fakhrullin, *Environ. Sci. Nano* 2 (2015) 54–59.
- [41] D. Peixoto, I. Pereira, M. Pereira-Silva, F. Veiga, M.R. Hamblin, Y. Lvov, M. Liu, A. C. Paiva-Santos, *Coord. Chem. Rev.* 440 (2021), 213956.
- [42] A.K. Gaharwar, L.M. Cross, C.W. Peak, K. Gold, J.K. Carrow, A. Brokesh, K. A. Singh, *Adv. Mater.* 31 (2019), 1900332.
- [43] N. Khatoon, M.Q. Chu, C.H. Zhou, *J. Mater. Chem. B* 8 (2020) 7335–7351.
- [44] D. Karatas, A. Tekin, F. Bahadır, M.S. Celik, *J. Mater. Chem. B* 5 (2017) 8070–8082.
- [45] J. Liao, Y. Qian, Z. Sun, J. Wang, Q. Zhang, Q. Zheng, S. Wei, N. Liu, H. Yang, *J. Phys. Chem. Lett.* 13 (2022) 8429–8435.
- [46] M.E. Awad, E. Escamilla-Roa, A. Borrego-Sánchez, C. Viseras, A. Hernández-Laguna, C.I. Sainz-Díaz, *Clay Min.* 54 (2019) 49–56.
- [47] C. Soriano-Correa, A. Pérez de la Luz, C.I. Sainz-Díaz, *J. Pharm. Sci.* 112 (2023) 798–807.
- [48] E.P. Rebitki, M. Darder, C.I. Sainz-Díaz, R. Carraro, P. Aranda, E. Ruiz-Hitzky, *Appl. Clay Sci.* 186 (2020), 105418.
- [49] J. Wang, Y. Meng, Z. Jiang, M.T. Sarwar, L. Fu, H. Yang, *Adv. Funct. Mater.* 33 (2023), 2210406.
- [50] Y. Yang, Y. Zhang, L. Wang, Z. Miao, K. Zhou, Q. Yang, J. Yu, X. Li, Y. Zhang, *Adv. Funct. Mater.* 32 (2022), 2200447.
- [51] A.M. Bieser, J.C. Tiller, *Macromol. Biosci.* 11 (2011) 526–534.
- [52] A.C. Neto, F. Guinea, N.M. Peres, K.S. Novoselov, A.K. Geim, *Rev. Mod. Phys.* 81 (2009) 109.
- [53] K.S. Novoselov, A.K. Geim, S.V. Morozov, D.-e Jiang, Y. Zhang, S.V. Dubonos, I. V. Grigorieva, A.A. Firsov, *Science* 306 (2004) 666–669.
- [54] X. Xu, C. Liu, Z. Sun, T. Cao, Z. Zhang, E. Wang, Z. Liu, K. Liu, *Chem. Soc. Rev.* 47 (2018) 3059–3099.
- [55] M. Heshami, Z. Tavangar, B. Taheri, *Appl. Surf. Sci.* 619 (2023), 156676.
- [56] J. Koo, M. Park, S. Hwang, B. Huang, B. Jang, Y. Kwon, H. Lee, *Phys. Chem. Chem. Phys.* 16 (2014) 8935–8939.
- [57] H.H. Wong, M. Sun, B. Huang, *2D Mater.* 8 (2021), 044009.
- [58] J. Li, A. Slassi, X. Han, D. Cornil, M.-H. Ha-Thi, T. Pino, D.P. Debecker, C. Colbeau-Justin, J. Arbiol, J. Cornil, M.N. Ghazzal, *Adv. Funct. Mater.* 31 (2021), 2100994.
- [59] S.H. North, E.H. Lock, C.R. Taitt, S.G. Walton, *Anal. Bioanal. Chem.* 397 (2010) 925–933.
- [60] A. Vaidyanathan, M. Mathew, S. Radhakrishnan, C.S. Rout, B. Chakraborty, *J. Phys. Chem. B* 124 (2020) 11098–11122.
- [61] R. Bhadoria, H.S. Chaudhary, *Int. J. Drug Deliv.* 3 (2011) 571.
- [62] G. Yıldız, M. Bolton-Warberg, F. Awaja, *Acta Biomater.* 131 (2021) 62–79.
- [63] K.M. Tripathi, T. Kim, D. Losic, T.T. Tung, *Carbon* 110 (2016) 97–129.
- [64] P. Singh, P.A. Sohi, M. Kahrizi, *Phys. E* 135 (2022), 114972.
- [65] A. Zhu, X. Luo, *J. Phys. Chem. B* 126 (2022) 151–160.
- [66] S.M. Aghaei, A. Aasi, S. Farhangdoust, B. Panchapakesan, *Appl. Surf. Sci.* 536 (2021), 147756.
- [67] A. Aasi, S. Mehdi Aghaei, B. Panchapakesan, *ACS Omega* 6 (2021) 4696–4707.
- [68] S. Nikmanesh, R. Safaiee, M.H. Sheikhi, *Surf. Interfaces* 29 (2022), 101658.
- [69] R. Majidi, M. Nadafan, *Phys. Lett. A* 384 (2020), 126036.
- [70] M.A. Sakr, K. Elgammal, A. Delin, M. Serry, *Sensors* 20 (2020) 145.
- [71] P. Lakhera, S. Singh, R. Mehla, V. Chaudhary, P. Kumar, S. Kumar, *IEEE Sens. J.* 22 (2022) 7572–7579.

- [72] F. Opoku, A.O. Osikoya, E.D. Dikio, P.P. Govender, *Diam. Relat. Mater.* 100 (2019), 107592.
- [73] Y. Yin, J. Cervenka, N.V. Medhekar, *J. Phys. Chem. Lett.* 8 (2017) 3087–3094.
- [74] J. Qasem, P. Pardeshi, A. Ingle, R. Karde, S. Ali, B. Lone, *J. Phys. Conf. Ser.* 2070 (2021), 012012.
- [75] S. Ali, B. Lone, *Mater. Today Proc.* 66 (2022) 1617–1622.
- [76] B. Li, Z.-G. Shao, *Appl. Surf. Sci.* 512 (2020), 145635.
- [77] S.J. Rodríguez, L. Makinistian, E.A. Albanesi, *Appl. Surf. Sci.* 419 (2017) 540–545.
- [78] N. Ding, X. Lu, C.-M.L. Wu, *Comput. Mater. Sci.* 51 (2012) 141–145.
- [79] Y. Badhe, R. Gupta, B. Rai, *RSC Adv.* 11 (2021) 3816–3826.
- [80] M.A. Sk, A. Ananthanarayanan, L. Huang, K.H. Lim, P. Chen, *J. Mater. Chem. C* 2 (2014) 6954–6960.
- [81] A. Karatay, D. Erdener, C. Gürçan, E.A. Yıldız, A. Yilmazer, B. Boyacioglu, H. Unver, M. Yıldız, A. Elmali, *J. Photochem. Photobiol. A* 426 (2022), 113741.
- [82] G. Potsi, A.B. Bourlinos, V. Mouselimis, K. Poláková, N. Chalmpes, D. Gournis, S. Kalytchuk, O. Tomaneac, P. Blonski, M. Medved, P. Lazar, M. Otyepka, R. Zboril, *Appl. Mater. Today* 17 (2019) 112–122.
- [83] Z. Liu, J.T. Robinson, X. Sun, H. Dai, *J. Am. Chem. Soc.* 130 (2008) 10876–10877.
- [84] W. Qin, X. Li, W.-W. Bian, X.-J. Fan, J.-Y. Qi, *Biomaterials* 31 (2010) 1007–1016.
- [85] W. Zhang, *Mol. Phys.* 120 (2022) e2129107.
- [86] A. Zaboli, H. Raissi, F. Farzad, H. Hashemzadeh, F. Fallahi, *Inorg. Chem. Commun.* 141 (2022), 109542.
- [87] F. Safdari, H. Raissi, M. Shahabi, M. Zaboli, *J. Inorg. Organomet. Polym. Mater.* 27 (2017) 805–817.
- [88] M. Mahdavi, F. Rahmani, S. Nouranian, *J. Mater. Chem. B* 4 (2016) 7441–7451.
- [89] P. Gong, L. Zhang, X-a Yuan, X. Liu, X. Diao, Q. Zhao, Z. Tian, J. Sun, Z. Liu, J. You, *Dyes Pigments* 162 (2019) 573–582.
- [90] A. Zaboli, H. Raissi, F. Farzad, H. Hashemzadeh, *J. Mol. Liq.* 301 (2020), 112435.
- [91] A. Alinejad, H. Raissi, H. Hashemzadeh, *J. Biomol. Struct. Dyn.* 38 (2020) 2737–2745.
- [92] Z. Shariatinia, A. Mazloom-Jalali, *J. Mol. Liq.* 273 (2019) 346–367.
- [93] X. Shen, Z. Wang, X.J. Gao, X. Gao, *Adv. Mater.*, <https://doi.org/10.1002/adma.202211151>.
- [94] Y. Lin, J. Ren, X. Qu, *Acc. Chem. Res.* 47 (2014) 1097–1105.
- [95] Y. Song, K. Qu, C. Zhao, J. Ren, X. Qu, *Adv. Mater.* 22 (2010) 2206–2210.
- [96] H. Sun, N. Gao, K. Dong, J. Ren, X. Qu, *ACS Nano* 8 (2014) 6202–6210.
- [97] A.A. Vernekar, G. Mugesh, *Chem. Eur. J.* 19 (2013) 16699–16706.
- [98] D. Wang, X. Song, P. Li, X.J. Gao, X. Gao, *J. Mater. Chem. B* 8 (2020) 9028–9034.
- [99] Y. Hu, X.J. Gao, Y. Zhu, F. Muhammad, S. Tan, W. Cao, S. Lin, Z. Jin, X. Gao, H. Wei, *Chem. Mater.* 30 (2018) 6431–6439.
- [100] M.S. Kim, S. Cho, S.H. Joo, J. Lee, S.K. Kwak, M.I. Kim, J. Lee, *ACS Nano* 13 (2019) 4312–4321.
- [101] M.S. Kim, J. Lee, H.S. Kim, A. Cho, K.H. Shim, T.N. Le, S.S.A. An, J.W. Han, M. I. Kim, J. Lee, *Adv. Funct. Mater.* 30 (2020), 1905410.
- [102] L. Jiao, W. Xu, Y. Zhang, Y. Wu, W. Gu, X. Ge, B. Chen, C. Zhu, S. Guo, *Nano Today* 35 (2020), 100971.
- [103] W. Ma, Y. Xue, S. Guo, Y. Jiang, F. Wu, P. Yu, L. Mao, *Chem. Commun.* 56 (2020) 5115–5118.
- [104] X. Bi, Q. Bai, L. Wang, F. Du, M. Liu, W.W. Yu, S. Li, J. Li, Z. Zhu, N. Sui, J. Zhang, *Nano Res.* 15 (2022) 1446–1454.
- [105] C. Zhang, L. Chen, Q. Bai, L. Wang, S. Li, N. Sui, D. Yang, Z. Zhu, *ACS Appl. Mater. Interfaces* 14 (2022) 27720–27732.
- [106] M. Głanowski, P. Wójcik, M. Prochner, T. Borowski, D. Lupa, P. Mielczarek, M. Oszajca, K. Świderek, V. Moliner, A.J. Bojarski, M. Szaleńiec, *ACS Catal.* 11 (2021) 8211–8225.
- [107] Z. Chen, Y. Yu, Y. Gao, Z. Zhu, *ACS Nano* 17 (2023) 13062–13080.
- [108] C. Zhang, Y. Yu, S. Shi, M. Liang, D. Yang, N. Sui, W.W. Yu, L. Wang, Z. Zhu, *Nano Lett.* 22 (2022) 8592–8600.
- [109] J. Zhuang, A.C. Midgley, Y. Wei, Q. Liu, D. Kong, X. Huang, *Adv. Mater.* (2023), 2210848.
- [110] Y. Li, R. Zhang, X. Yan, K. Fan, *J. Mater. Chem. B* 11 (2023) 6466–6477.
- [111] Y. Yu, Y. Jiang, C. Zhang, Q. Bai, F. Fu, S. Li, L. Wang, W.W. Yu, N. Sui, Z. Zhu, *ACS Mater. Lett.* 4 (2022) 2134–2142.
- [112] S. Roy, X. Zhang, A.B. Puthirath, A. Meiyazhagan, S. Bhattacharyya, M. M. Rahman, G. Babu, S. Susarla, S.K. Saju, M.K. Tran, L.M. Sassi, M.A.S.R. Saadi, J. Lai, O. Sahin, S.M. Sajadi, B. Dharmarajan, D. Salpekar, N. Chakinal, A. Baburaj, X. Shuai, A. Adumbumkulath, K.A. Miller, J.M. Gayle, A. Ajnsztajn, T. Prasankumar, V.V.J. Harikrishnan, V. Ojha, H. Kannan, A.Z. Khater, Z. Zhu, S. A. Iyengar, P.Ad.S. Autreto, E.F. Oliveira, G. Gao, A.G. Birdwell, M.R. Neupane, T. G. Ivanov, J. Taha-Tijerina, R.M. Yadav, S. Areppalli, R. Vajtai, P.M. Ajayan, *Adv. Mater.* 33 (2021), 2101589.
- [113] M. Rafique, M.A. Unar, I. Ahmed, A.R. Chachar, Y. Shuai, *J. Phys. Chem. Solids* 118 (2018) 114–125.
- [114] H. Alinezhad, M.D. Ganji, E. Soleymani, M. Tajbakhsh, *Appl. Surf. Sci.* 422 (2017) 56–72.
- [115] S. Bhai, B. Ganguly, *Phys. Chem. Chem. Phys.* 24 (2022) 829–841.
- [116] B. Roondhe, P.K. Jha, *J. Mater. Chem. B* 6 (2018) 6796–6807.
- [117] H. Vovusha, R.G. Amorim, R.H. Scheicher, B. Sanyal, *RSC Adv.* 8 (2018) 6527–6531.
- [118] S. Rani, S.J. Ray, *Carbon* 173 (2021) 493–500.
- [119] N. Ding, X. Chen, C.-M.L. Wu, H. Li, *Phys. Chem. Chem. Phys.* 15 (2013) 10767–10776.
- [120] J.D. Watson, F.H.C. Crick, *Nature* 171 (1953) 737–738.
- [121] F.A.L. de Souza, R.G. Amorim, W.L. Scopel, R.H. Scheicher, *Nanoscale* 9 (2017) 2207–2212.
- [122] F.A.L. de Souza, G. Sivaraman, M. Fyta, R.H. Scheicher, W.L. Scopel, R. G. Amorim, *Nanoscale* 12 (2020) 18289–18295.
- [123] S. Baber, R.N.E. Malein, P. Khatri, P.S. Keatley, S. Guo, F. Withers, A.J. Ramsay, I. J. Luxmoore, *Nano Lett.* 22 (2022) 461–467.
- [124] F. Farzad, H. Hashemzadeh, *J. Mol. Graph. Modell.* 98 (2020), 107613.
- [125] A.M. Sultan, Z.E. Hughes, T.R. Walsh, *Langmuir* 30 (2014) 13321–13329.
- [126] E.G. Brandt, A.P. Lyubartsev, *J. Phys. Chem. C* 119 (2015) 18126–18139.
- [127] E. Darve, A. Pohorille, *J. Chem. Phys.* 115 (2001) 9169–9183.
- [128] A. Laio, M. Parrinello, *Proc. Natl. Acad. Sci.* 99 (2002) 12562–12566.
- [129] F. Wang, D.P. Landau, *Phys. Rev. Lett.* 86 (2001) 2050.
- [130] G.M. Torrie, J.P. Valleau, *J. Comput. Phys.* 23 (1977) 187–199.
- [131] M.J. McGrath, I.-F.W. Kuo, S. Hayashi, S. Takada, *J. Am. Chem. Soc.* 135 (2013) 8908–8919.
- [132] M. Vatanparast, Z. Shariatinia, *J. Mol. Graph. Modell.* 89 (2019) 50–59.
- [133] P.A. Maleki, E. Nemati-Kande, A.A. Saray, *ChemistrySelect* 6 (2021) 6119–6131.
- [134] Y. Liu, G. Zhang, *ChemistrySelect* 7 (2022), e202103913.
- [135] N. Rohraizad, C.C. Mayorga-Martinez, Z. Sofer, M. Pumera, *ACS Appl. Mater. Interfaces* 9 (2017) 40697–40706.
- [136] H. Hu, A. Zavabeti, H. Quan, W. Zhu, H. Wei, D. Chen, J.Z. Ou, *Biosens. Bioelectron.* 142 (2019), 111573.
- [137] M. Xiao, S. Wei, J. Chen, J. Tian, C.L. Brooks III, E.N.G. Marsh, Z. Chen, *J. Am. Chem. Soc.* 141 (2019) 9980–9988.
- [138] K.F. Mak, C. Lee, J. Hone, J. Shan, T.F. Heinz, *Phys. Rev. Lett.* 105 (2010), 136805.
- [139] C. Ataca, S. Ciraci, *J. Phys. Chem. C* 115 (2011) 13303–13311.
- [140] H. Yang, Y. Liu, C. Gao, L. Meng, Y. Liu, X. Tang, H. Ye, *J. Phys. Chem. C* 123 (2019) 30949–30957.
- [141] Y. Lei, D. Butler, M.C. Lucking, F. Zhang, T. Xia, K. Fujisawa, T. Granzier-Nakajima, R. Cruz-Silva, M. Endo, H. Terrones, M. Terrones, A. Ebrahimi, *Sci. Adv.* 6 (2020), eabc4250.
- [142] J.D. Benck, T.R. Hellstern, J. Kibsgaard, P. Chakthranont, T.F. Jaramillo, *ACS Catal.* 4 (2014) 3957–3971.
- [143] K. Lu, J. Liu, X. Dai, L. Zhao, Y. Yang, H. Li, Y. Jiang, *RSC Adv.* 12 (2022) 798–809.
- [144] A. Gupta, T.B. Rawal, C.J. Neal, S. Das, T.S. Rahman, S. Seal, *2D Mater.* 4 (2017), 025077.
- [145] T. Liu, Z. Cui, X. Li, H. Cui, Y. Liu, *ACS Omega* 6 (2021) 988–995.
- [146] A. Verma, B.C. Yadav, *ACS Appl. Nano Mater.* 6 (2023) 5493–5507.
- [147] L. Li, Z.-W. Tian, W.-H. Zhao, Q.-C. Zheng, R. Jia, *Appl. Surf. Sci.* 614 (2023), 156257.
- [148] L. Wang, F. Gao, A. Wang, X. Chen, H. Li, X. Zhang, H. Zheng, R. Ji, B. Li, X. Yu, J. Liu, Z. Gu, F. Chen, C. Chen, *Adv. Mater.* 32 (2020), 2005423.
- [149] T. Wang, X. Zhang, L. Mei, D. Ma, Y. Liao, Y. Zu, P. Xu, W. Yin, Z. Gu, *Nanoscale* 12 (2020) 8415–8424.
- [150] Y. Li, E.C. Moy, A.A. Murthy, S. Hao, J.D. Cain, E.D. Hanson, J.G. DiStefano, W. H. Chae, Q. Li, C. Wolverton, X. Chen, V.P. Dravid, *Adv. Funct. Mater.* 28 (2018), 1704863.
- [151] F. Cao, L. Zhang, H. Wang, Y. You, Y. Wang, N. Gao, J. Ren, X. Qu, *Angew. Chem. Int. Ed.* 58 (2019) 16236–16242.
- [152] L. Feng, L. Zhang, S. Zhang, X. Chen, P. Li, Y. Gao, S. Xie, A. Zhang, H. Wang, *ACS Appl. Mater. Interfaces* 12 (2020) 17547–17556.
- [153] Q. Zhu, H. Zhang, Y. Li, H. Tang, J. Zhou, Y. Zhang, J. Yang, *J. Mater. Sci.* 57 (2022) 8100–8112.
- [154] G. Emilsson, E. Röder, B. Malekian, K. Xiong, J. Manzi, F.-C. Tsai, N.-J. Cho, M. Bally, A. Dahlén, *Front. Chem.* 7 (2019).
- [155] N. Singh, M.A. Savanur, S. Srivastava, P.D. Silva, G. Mugesh, *Nanoscale* 11 (2019) 3855–3863.
- [156] X. Zhang, S. Zhang, Z. Yang, Z. Wang, X. Tian, R. Zhou, *Nanoscale* 13 (2021) 12613–12622.
- [157] C. Du, Q. Zhang, Z. Lin, B. Yan, C. Xia, G. Yang, *Appl. Catal. B* 248 (2019) 193–201.
- [158] M.N. Gjerding, A. Taghizadeh, A. Rasmussen, S. Ali, F. Bertoldo, T. Deilmann, N. R. Knosgaard, M. Kruse, A.H. Larsen, S. Manti, *2D Mater.* 8 (2021), 044002.
- [159] Z. Wang, J. Wu, J.-J. Zheng, X. Shen, L. Yan, H. Wei, X. Gao, Y. Zhao, *Nat. Commun.* 12 (2021) 6866.
- [160] S. Anju, P.V. Mohanan, *Synth. Met.* 271 (2021), 116610.
- [161] M.H. Mohammed, F.H. Hanooon, *Comput. Theor. Chem.* 1190 (2020), 112999.
- [162] W. Liang, X. Luo, *J. Phys. Chem. C* 124 (2020) 8279–8287.
- [163] J. Chen, C. Wang, H. Li, X. Xu, J. Yang, Z. Huo, L. Wang, W. Zhang, X. Xiao, Y. Ma, *Molecules* 28 (2023) 200.
- [164] W. Chen, W. Pan, J. Wang, L. Cheng, J. Wang, L. Song, Y. Hu, X. Ma, *WIREs Nanomed. Nanobi.* 14 (2022), e1750.
- [165] W. Tao, N. Kong, X. Ji, Y. Zhang, A. Sharma, J. Ouyang, B. Qi, J. Wang, N. Xie, C. Kang, H. Zhang, O.C. Farokhzad, J.S. Kim, *Chem. Soc. Rev.* 48 (2019) 2891–2912.
- [166] J. Shao, H. Xie, H. Huang, Z. Li, Z. Sun, Y. Xu, Q. Xiao, X.-F. Yu, Y. Zhao, H. Zhang, H. Wang, P.K. Chu, *Nat. Commun.* 7 (2016) 12967.
- [167] S. Kansara, J. Shah, Y. Sonvane, S.K. Gupta, *Chem. Phys. Lett.* 715 (2019) 115–122.
- [168] T. Xue, W. Liang, Y. Li, Y. Sun, Y. Xiang, Y. Zhang, Z. Dai, Y. Duo, L. Wu, K. Qi, B. N. Shivanjanu, L. Zhang, X. Cui, H. Zhang, Q. Bao, *Nat. Commun.* 10 (2019) 28.
- [169] A. Ayatollahi, M.R. Roknabadi, M. Behdani, N. Shahtahmassebi, B. Sanyal, *Phys. E* 127 (2021), 114498.
- [170] H.H. Gürel, B. Salmankurt, *Biosensors* 11 (2021) 59.
- [171] S. Sabokdast, A. Horri, Y.T. Azar, M. Momeni, M.B. Tavakoli, *Bioelectrochemistry* 138 (2021), 107721.

- [172] H. Guo, K. Zheng, H. Cui, J. Yu, L.-Q. Tao, X. Li, C. Liao, L. Xie, X. Chen, *Appl. Surf. Sci.* 532 (2020), 147451.
- [173] S. Ebrahimi Loushab, M.R. Benam, R.P. Shahri, J. Baedi, A. Feyzi, *Phys. B* 618 (2021), 412771.
- [174] V. Nagarajan, N. Srividya, R. Chandiramouli, *FlatChem* 30 (2021), 100293.
- [175] V. Nagarajan, S. Sundar, R. Chandiramouli, *Comput. Theor. Chem.* 1205 (2021), 113426.
- [176] H. Hashemzadeh, H. Raissi, *J. Mol. Liq.* 291 (2019), 111346.
- [177] H. Hashemzadeh, H. Raissi, *J. Biomol. Struct. Dyn.* 39 (2021) 5613–5618.
- [178] A. Tariq, S. Nazir, A.W. Arshad, F. Nawaz, K. Ayub, J. Iqbal, *RSC Adv.* 9 (2019) 24325–24332.
- [179] S.A. Mian, S.U. Khan, A. Hussain, A. Rauf, E. Ahmed, J. Jang, *Cancers* 14 (2022) 545.
- [180] K. Jaffar, S. Riaz, Q.Q. Afzal, M. Perveen, M.A. Tahir, S. Nazir, J. Iqbal, Z. A. Alrowaili, S. ben Ahmed, M.S. Al-Buriahi, *Comput. Theor. Chem.* 1212 (2022), 113724.
- [181] J. Rafique, Q.Q. Afzal, M. Perveen, J. Iqbal, M.S. Akhter, S. Nazir, M.S. Al-Buriahi, S. Alomairy, Z.A. Alrowaili, *J. Taibah Univ. Sci.* 16 (2022) 31–46.
- [182] H. Hashemzadeh, H. Raissi, *J. Biomed. Mater. Res. Part A* 109 (2021) 1912–1921.
- [183] L. Razavi, H. Raissi, H. Hashemzadeh, F. Farzad, *J. Biomol. Struct. Dyn.* 39 (2021) 3892–3899.
- [184] L. Razavi, H. Raissi, F. Farzad, *J. Mol. Graph. Modell.* 106 (2021), 107930.
- [185] H. Karim, Shahnaz, M. Batool, M. Yaqub, M. Saleem, M.A. Gilani, S. Tabassum, *Appl. Surf. Sci.* 596 (2022), 153618.
- [186] T. Mahboobi, M.R. Zardoost, M.R. Toosi, *J. Mol. Model.* 26 (2020), 269.
- [187] S. Kim, T.Y. Ohulchansky, H.E. Pudavar, R.K. Pandey, P.N. Prasad, *J. Am. Chem. Soc.* 129 (2007) 2669–2675.
- [188] J. Liu, C. Zhang, T.W. Rees, L. Ke, L. Ji, H. Chao, *Coord. Chem. Rev.* 363 (2018) 17–28.
- [189] M. Ge, H. Guo, M. Zong, Z. Chen, Z. Liu, H. Lin, J. Shi, *Angew. Chem. Int. Ed.* 62 (2023), e202215795.
- [190] D. Xu, H. Lin, W. Qiu, M. Ge, Z. Chen, C. Wu, Y. You, X. Lu, C. Wei, J. Liu, X. Guo, J. Shi, *Biomaterials* 278 (2021), 121172.
- [191] J. Zhang, Q. Bai, X. Bi, C. Zhang, M. Shi, W.W. Yu, F. Du, L. Wang, Z. Wang, Z. Zhu, N. Sui, *Nano Today* 43 (2022), 101429.
- [192] T. Wang, Q. Bai, Z. Zhu, H. Xiao, F. Jiang, F. Du, W.W. Yu, M. Liu, N. Sui, *Chem. Eng. J.* 413 (2021), 127537.
- [193] T. Liu, J. Zhang, P. Ouyang, L. Fu, H. Yang, *Appl. Clay Sci.* 215 (2021), 106303.



**Yinyin Qian** is currently a Ph.D. candidate in Materials Science and Engineering in the Engineering Research Center of Nano-Geomaterials of Ministry of Education at China University of Geoscience (Wuhan) under the supervision of Prof. Huaming Yang. She received her M.S. degree in polymer chemistry and physics from Heilongjiang University in 2021. Her main research interests are theoretical calculations of clay mineral materials for biological applications.



**Huaming Yang** is a professor at the Engineering Research Center of Nano-Geomaterials of Ministry of Education at China University of Geosciences (Wuhan), and in the School of Minerals Processing and Bioengineering at Central South University, China. He completed his Ph.D. at Central South University of Technology in 1998, and went to the University of Bristol as a visiting professor from 2008 to 2009. He was awarded the National Science Fund for Distinguished Young Scholars in China. His research interests involve the synthesis strategy and application of energy, environmental and biomedical materials from minerals, and the microstructures of functional materials at the atomic-molecular level.